Title: New resorbable Ca-Mg-Zn-Yb-B-Au alloys : structural and corrosion resistance characterization

Author: Dawid Szyba, Anna Bajorek, Dorota Babilas, László Temleitner, Dariusz Łukowiec, Rafał Babilas

Citation style: Szyba Dawid, Bajorek Anna, Babilas Dorota, Temleitner László, Łukowiec Dariusz, Babilas Rafał. (2022). New resorbable Ca-Mg-Zn-Yb-B-Au alloys : structural and corrosion resistance characterization. "Materials and Design" (2022), Vol. 213, art. no. 110327, s. 1-16. DOI: 10.1016/j.matdes.2021.110327

Materials & Design 213 (2022) 110327

Contents lists available at ScienceDirect

Materials & Design

journal homepage: www.elsevier.com/locate/matdes

New resorbable Ca-Mg-Zn-Yb-B-Au alloys: Structural and corrosion resistance characterization

Dawid Szyba [a,*], Anna Bajorek [b], Dorota Babilas [c], László Temleitner [d], Dariusz Łukowiec [a], Rafał Babilas [a,*]

[a] Department of Engineering Materials and Biomaterials, Silesian University of Technology, Konarskiego 18a St, Gliwice 44-100, Poland
[b] A. Chelkowski Institute of Physics, University of Silesia in Katowice, 75 Pułku Piechoty 1 St, 41-500 Chorzów, Poland
[c] Department of Inorganic, Analytical Chemistry and Electrochemistry, Silesian University of Technology, B. Krzywoustego 6 St, 44-100 Gliwice, Poland
[d] Wigner Research Centre for Physics, Konkoly Thege út 29-33, H-1121 Budapest, Hungary

HIGHLIGHTS

- The CaMgZnYbBAu alloys were studied using novel spectroscopic and microscopic techniques.
- The improved biocorrosion resistance in Ringer solution was stated.
- The corrosion mechanism includes anodic dissolution, hydroxide precipitation, and corrosion propagation.
- Novel bioresorbable materials for biomedical applications were proposed.

GRAPHICAL ABSTRACT

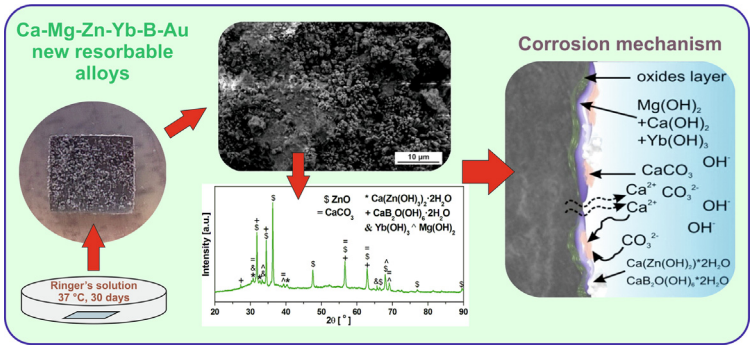

ARTICLE INFO

Article history:
Received 11 October 2021
Revised 12 December 2021
Accepted 14 December 2021
Available online 16 December 2021

Keywords:
Ca-based alloys
Bioresorbable materials
Electrochemical study
Hydrogen evolution
Biocorrosion behavior
Mechanical properties

ABSTRACT

New resorbable $Ca_{32}Mg_{12}Zn_{38}Yb_{18-2x}B_xAu_x$ (x = 1,2) alloys were designed and prepared in order to verify their use for medical applications as potential short-term implants. Their amorphous structure containing some crystalline phases (CaZn, CaZn2 and MgZn) was determined by X-ray and neutron diffraction and electron microscopy methods. The biocorrosion behavior of the plates was tested by hydrogen evolution measurements, immersion, electrochemical polarization tests, and electrochemical impedance spectroscopy in Ringer's solution at 37 °C. The corrosion analysis was also supplemented by X-ray diffraction, photoelectron, and ICP-AES spectroscopy. The corrosion resistivity measurements revealed that the alloys manifest enhanced corrosion resistance. The corrosion current density for $Ca_{32}Mg_{12}Zn_{38}Yb_{18-2x}B_xAu_x$ (x = 1, 2) alloys were 18.46 and 8.79 µA/cm^2, which is lower than for pure Mg (47.85 µA/cm^2) and Zn (33.96 µA/cm^2). A decreasing tendency for hydrogen to evolve as a function of time was noted. The hydrogen evolution did not exceed 1 ml/cm^2 over 1 h and average corrosion rate is calculated as 0.32 g/m^2 · h for $Ca_{32}Mg_{12}Zn_{38}Yb_{14}B_2Au_2$ alloy after 312 h. The corrosion mechanism of the alloys includes an anodic dissolution, a hydroxide precipitation, corrosion product layer formation and corrosion propagation stage.

1. Introduction

Nowadays, biodegradable metals are a promising class of biomedical materials that have received great attention because of their use as temporary medical implants [1]. The dominant class

* Corresponding authors.
E-mail addresses: dawid.szyba@polsl.pl (D. Szyba), rafal.babilas@polsl.pl (R. Babilas).

https://doi.org/10.1016/j.matdes.2021.110327
0264-1275/

of materials used for such implants are magnesium alloys. They are used as orthopedic items to find applicability in the bones of hand or foot, moreover, magnesium is a fundamental element in the human body [2].

A new family of biomaterials for potential orthopedic implants is based on a group of biodegradable alloys containing calcium (Ca) and magnesium (Mg), with the addition of zinc (Zn), ytterbium (Yb), boron (B) and gold (Au) [3]. Ca is a major component in human bone and Ca ions are beneficial for bone curing [4]. In turn, Zn is reported as fundamental element in the human body and is safe for biomedical uses; it enhances the corrosion resistance by the formation of a passive film on the alloys surface [5].

Au is known as the most inert of metals with immunity to corrosion [6]. It can be used in many medical applications. Au implants are used in reconstructive surgery, drug delivery microchips, treatment of rheumatoid arthritis, and endovascular stents [7]. In case of stents, it is used to coat them to increase their biocompatibility and hemocompatibility [8]. Moreover, gold in alloys with other precious and non-precious metals is also used for dental items as crowns and bridges for the repair of broken teeth [9].

Metalloids such as B can slow down the rate of corrosion of Fe-, Co– and Cu-based alloys in NaCl solution [10–12]. From the other side, B is a biocompatible element with a positive effect on the growth and strengthening of bones and is required for the maintenance of human health [13]. In addition, small amounts of B can be used in treating arthritis as well as osteoarthritis [14–16].

B in the human body also influences the excretion of Ca and Mg [17–19]. The supplementation of B using boric acid influences a possible mechanism that promotes the proliferation and differentiation of mammalian osteoblastic cells in vitro [20]. Therefore, B compounds enhance bone growth, and the regeneration of bone is dependent on angiogenesis that is affected by B [21,22].

Enhanced growth of human osteoblast-like cells on boron-doped nanocrystalline diamond thin films was reported by Grausova et al. [23]. After a seeding time of three days, the cell population density on doped and undoped nanocrystalline diamond films increased more significantly than the cell population in a control group. The amount of cells on undoped films was significantly smaller than on those doped by boron.

Dai et al. [24] reported the influence of $Yb3^{+}$ on bone marrow stromal cells (BMSCs) to explain the mechanism of bone metabolism and propose more rational application of Yb-based compounds in medical uses. Their experiment showed that Yb^{3+} had no effect on BMSC viability at a concentration of 1×10^{-7} mol/L. As a result of a slightly higher Yb^{3+} concentration in the range of $1 \times 10^{-6} - 1 \times 10^{-4}$ mol/L, a positive effect on BMSC viability was also noticed.

Cytotoxicity tests of $Mg_{66}Zn_{30}Ca_{4-x}Yb_x$ (x = 0, 2, 4) and $Mg_{70-x}Zn_{30}Yb_x$ (x = 6, 10) glassy ribbons with variable chemical composition were also provided by Wang et al. [25]. The tests were conducted directly and indirectly by preparing extracts with a concentration of 60% and by an adhesion test. The extract exhibited good cell compatibility with fibroblasts and osteoblasts. The adhesion of cells was also tested on ribbons with and without addition of Yb. The number of cells in the adhesion test were comparable to that in the control group and on the ribbon with the addition of Yb. Samples without any addition of Yb revealed an 80% decrease in cell number on their surface compared to a control group and samples with Yb addition.

Moreover, Jiao et al. [26] used MG63 culture cells to evaluate the cytocompatibility of the $Ca_{32}Zn_{38}Mg_{12}Yb_{18}$ alloy and pure Mg. The MG63 cells on the surface of the alloy with the addition of Yb were still in a healthy, elongated spindle shape. In the case of MG63 cells cultured on the Mg surface a round shape, showing an unhealthy state, was noted.

In view of the above, in this study, the influence of Yb, B, and Au addition in Ca-Mg-Zn-(Yb,B,Au) alloys on the amorphous structure forming, hydrogen evolution, corrosion rate, biocorrosion behavior and mechanical properties was studied. The corrosion mechanism in an artificial physiological fluid as Ringer's solution at 37 °C was proposed and discussed. Presented results can be helpful to determine novel bioresorbable materials with unique properties for biomedical applications e.g. short-term implants. The examination of the Ca-Mg-Zn-(Yb,B,Au) alloys should fill the gap in scientific scope, which includes the structure and properties investigations of biomaterials based on Ca.

2. Materials and methods

2.1. Preparation of the samples

The investigations were conducted on $Ca_{32}Mg_{12}Zn_{38}Yb_{18-2x}B_xAu_x$ (x = 1, 2 at.%) as-cast alloys. The base alloys were produced by the induction melting of elements Ca, Mg, Zn, Yb and Au (with a purity of 99.90%, 99.90%, 99.90%, 99.95%, 99.90%, respectively) in a ceramic crucible. The pre-ingots were then re-melted with pure B (99.90%) due to its higher melting temperature than the other elements. Subsequently, the cylindrical ingots with diameter of 30 mm were obtained. At the first stage, metals with similar melting temperature were melted: Ca (842 °C), Yb (824 °C) and Au (1064 °C). Next, Mg (650 °C) and Zn (419 °C) were added. The B was added once the five-component melt was obtained. The Ca, Mg, Zn, Yb, Au elements had a form of pieces, except B, which was used in a powder state to increase its solubility in the molten prealloy. Both alloys were cast under an inert atmosphere by purging the chamber with Ar (99.99%) to provide air reduction. The cylinder-shaped ingots were cut into small pieces and then placed in a quartz crucible. The induction melted pieces were injected into a copper mold and rapidly cooled plates with a length and a width of 10 mm and a thickness of 1 mm were cast [27,28].

2.2. Experimental methodology

A schematic representation of research methodology used in this work is shown in Fig. 1. The characterization methodology of the fabricated Ca-Mg-Zn-Yb-B-Au alloys includes chemical composition analysis, structural characterization, mechanical properties, and corrosion resistance examination.

Analysis of the chemical composition was provided by the JEOL JXA 8230 X-ray microanalysis. An accelerating voltage of 15 kV was used, with an electron beam current of 30nA. Quantitative analysis of the chemical composition and elemental distribution maps were carried out using the wavelength dispersion method (WDS). The size of the analyzed area, resulting from the characteristics of the electron beam and the area of X-ray excitation, is in the range of 1 μm^2. As standards in the quantitative analysis, the following were used: pure Zn, wollastonite ($CaSiO_3$) as the calcium standard, magnesium oxide (MgO) as the magnesium standard, ytterbium fluoride (YbF_3) as the ytterbium standard, lanthanum boride (LaB_6) as the boron standard and pure Au.

The structure of the plates in their as-cast state and after corrosion tests was analyzed by X-ray diffraction (XRD) in the reflection mode using a diffractometer with a Cu Kα radiation source (wavelength λ = 0.154 nm). The neutron diffraction (ND) data for $Ca_{32}Mg_{12}Zn_{38}Yb_{16}B_1Au_1$ plate in the as-cast state was collected using the neutron powder diffractometer MTEST at Budapest Research Center with the neutron wavelength λ = 0.111 nm.

The microstructure of alloys were described on the basis of light microscopy images in bright-field carried out by Zeiss Axio Observer. High-resolution transmission electron microscopy (HRTEM)

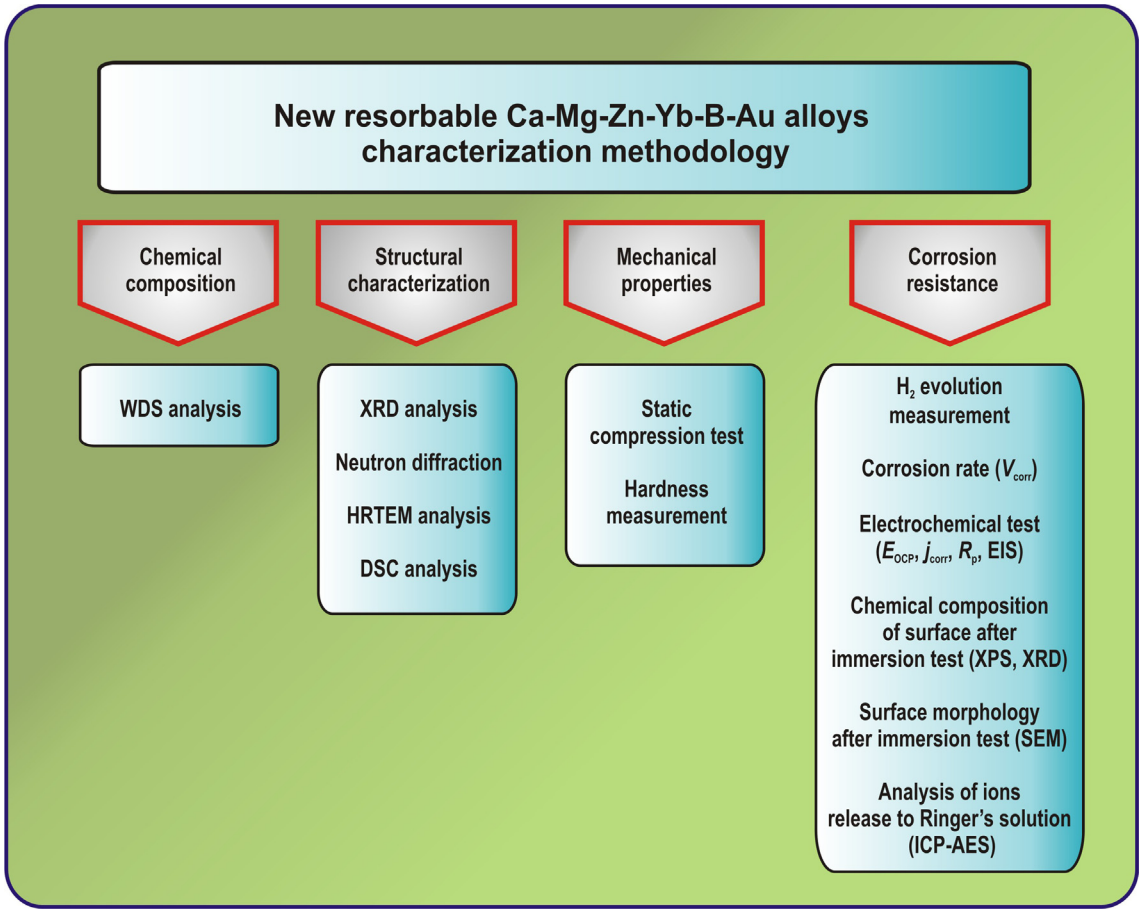

Fig. 1. Flow chart of the research methodology.

observations of plates were made using S/TEM TITAN 80–300 FEI microscope at the operating voltage of 300 kV. Differential scanning calorimetry (DSC) was performed using a 20 K/min heating rate under a helium protective atmosphere. The glass-transition temperature (T_g), onset crystallization temperature (T_x), and peak crystallization temperature (T_p) were determined for the examined plates.

As a part of the evaluation of the mechanical properties, static compression tests and hardness measurements were carried out. Non-standard compression tests of the alloys were performed using a ZWICK 100 testing machine at room temperature. The samples were square plates of side 3 mm and thickness 1 mm. For each alloy, 3 compression tests were performed, and the average compressive strength was taken. Microhardness tests were carried out using the Vickers method in accordance with the PN-EN ISO 6507–1:2007 standard on the Future-Tech FM-700 instrument using the automatic hardness FM-ARS 9000 testing system. Measurements were conducted with a load of 100 g (0.98 N). The impact time of the indenter on the sample surface was 15 s. The tests were carried out on 9 different areas of one specimen (total of 9 measurements per sample).

Electrochemical measurements were conducted using an Autolab 302 N workstation containing a glass corrosion cell. An alloy sample was used as the working electrode, a saturated calomel electrode (SCE) was used as the reference electrode, and a platinum rod was used as the counter electrode. The potentiodynamic curves were recorded over a potential range from E_{OCP} −250 mV to E_{OCP} + 250 mV, a scan rate was 1 mV s^{-1}, and the open-circuit potential (E_{OCP}) variation was collected for 3600 s. The corrosion parameters, such as the corrosion potential (E_{corr}) and corrosion current density (j_{corr}), were determined using the Tafel extrapolation method using both cathodic and anodic branches of the polarization curves [29–31]. The polarization resistance (R_p) was calculated according to equation:

$$R_p = \frac{1}{2.303(\frac{1}{\beta_a} + \frac{1}{\beta_c})j_{corr}} \quad (1)$$

where β_a and β_c are the anodic and cathodic Tafel slopes, respectively calculated from the Tafel extrapolation [29].

To complete the polarization measurements, electrochemical impedance spectroscopy (EIS) was carried out at open-circuit potentials with a potential amplitude adjusted at 5 mV over a frequency range of 10^5 –10^{-2} Hz. EIS data were analyzed by using NOVA version 1.11.2 software. An equivalent circuit was proposed by using "Fit and Simulation" tool. Both EIS and potentiodynamic polarization measurements were conducted in duplicate. Chi-square (χ^2) values were determined. The electrochemical polarization and immersion tests were conducted in Baxter Ringer's solution (8.6 g/dm^3 NaCl, 0.3 g/dm^3 KCl, 0.48 g/dm^3 $CaCl_2{\cdot}6H_2O$) at 37 °C.

Hydrogen evolution was also monitored for both alloys during immersion for a period of 30 days, with measurements being taken at 24 h intervals. Samples with dimensions of 10 × 10 × 1 mm were used. The bubbles of H_2 generated from the samples immersed in solution were collected using a funnel and a burette above the sample, and the volume of hydrogen evolved was calculated using the method presented in ref [32]. The immersion tests were also conducted to calculate the corrosion rate (V_{corr}, g/m^2·h) according to equation [33]:

$$V_{corr} = \frac{\Delta m}{S \cdot t} \quad (2)$$

where Δm is difference in sample mass before and after the corrosion test (g), S – sample area (m^2),

t – immersion time (h).

Previously corroded samples were analyzed by X-ray photoelectron spectroscopy (XPS) with the use of a PHI 5700/660 Physical Electronics spectrometer. The XPS spectra were collected using monochromatic Al $K\alpha$ (1486.6 eV) X-ray radiation under ultra-high vacuum (10^{-10} Torr). Depth profile (DP-XPS) analysis was performed during cyclic ion etching with an $Ar^{+\circ}$beam of 1.5 kV. In each cycle, the argon beam was applied for 15 min and afterwards the core level lines for elements having the highest photoemission cross-section were acquired. The whole procedure was repeated giving a final sputtering time of 240 min. All the determined spectra were related to the peak for the C1s orbital. The survey spectra were collected with a pass energy of 187.85 eV and a 0.8 eV/step, while all core level lines were measured with a pass energy of 23.5 eV and a resolution of 0.1 eV. XPS data analysis was carried out using MultiPak 9.4 software. The peak assignment and identification of chemical states was done based on MultiPak internal database and NIST database.

A Carl Zeiss Supra 35 scanning electron microscope (SEM) was used to determine changes in the surface morphology of samples after 168 and 720 h of immersion.

The concentrations of Ca, Mg, Zn, Yb, B and Au in saline Ringer's solutions before and after the immersion test were determined using the inductively coupled plasma atomic emission spectrometer Varian 710-ES (Santa Clara, CA, USA) equipped with the OneNeb nebulizer and twister glass spray chamber. The apparatus measuring parameters and selected emission lines are presented in Table 1. The emission lines precision ensues from the spectrometer resolution, and it is also important due to minimizing spectral interferences and the identification of the elements.

The concentrations of each element were obtained using the calibration curve method. The calibration curves were prepared using single element standard solutions of 1 mg/mL (Merck Millipore, Germany) and a matrix, which was the Ringer's solution with the same concentration as in the measured samples. The Millipore Elix 10 system was used to prepare deionized water. The calibration curves were created by measuring the maximum intensity for each standard at the peak maxima. The presented results constituted an average of the element concentrations obtained for all applied analytical lines and for the three replicates of each sample. The standard deviation was not exceeding 1.5%.

3. Results and discussion

The results of the chemical compositions of the $Ca_{32}Mg_{12}Zn_{38}Yb_{18-2x}B_xAu_x$ (x = 1, 2) alloys determined by wavelength dispersion analysis (WDS) are given in Table 2. It can be noticed that the Ca content of the as-cast samples is very close to the nominal composition of the alloys indicating an acceptable casting procedure.

XRD analysis of $Ca_{32}Mg_{12}Zn_{38}Yb_{18-2x}B_xAu_x$ (x = 1, 2) plates allowed broad halo and diffraction lines arising from crystalline phases to be detected (Fig. 2). Therefore, the XRD pattern of $Ca_{32}Mg_{12}Zn_{38}Yb_{16}B_1Au_1$ suggested the presence of crystalline phases such as CaZn (PDF 41–0881, Cmcm), CaZn2 (PDF 28–0257, Imma), and MgZn (PDF 40–1334, R) embedded in the amorphous matrix within the resolution limits of XRD. A similar phase composition was observed in the case of $Ca_{32}Mg_{12}Zn_{38}Yb_{14}B_2Au_2$ alloy, where a higher quantity of the crystalline phase was noted. However, other diffraction examination supporting the XRD results, neutron diffraction of the $Ca_{32}Mg_{12}Zn_{38}Yb_{16}B_1Au_1$ plate indicated the appearance of crystalline peaks on the broad diffraction lines (Fig. 3). A combined neutron and XRD study allowed to detect refined structure of tested material. Neutron diffraction pattern determined some crystalline-amorphous structure of studied plate. The differences in ND diffraction spectra come from higher measuring accuracy of neutron diffraction method. Reflections come from crystalline phases can be much better visible.

Fig. 4 shows HRTEM micrographs (Fig. 4a, c) and the corresponding selected area electron diffraction (SAED) patterns (Fig. 4b,d) of the $Ca_{32}Mg_{12}Zn_{38}Yb_{18-2x}B_xAu_x$ (x = 1, 2) plates. The SAED patterns for the x = 1 plate (Fig. 4b) show reflections indicating the formation of CaZn (Cmcm), CaZn2 (Imma) and MgZn (R) crystalline phases. For the sample x = 2, the diffraction patterns (Fig. 4d) present diffused diffraction rings and diffraction spots indicating the formation of CaZn and CaZn2 crystals within an amorphous matrix.

Thermal properties of the as-cast $Ca_{32}Mg_{12}Zn_{38}Yb_{18-2x}B_xAu_x$ (x = 1, 2) plates were determined by DSC measurements at a constant heating rate of 20 K/min. The glass-transition temperature (T_g), crystallization onset temperature (T_x) and peak crystallization temperature (T_p) are marked by arrows on the DSC curve shown in Fig. 5. The DSC curve of $Ca_{32}Mg_{12}Zn_{38}Yb_{16}B_1Au_1$ plate reveals that the T_g occurs at 398 K and the T_x is 430 K. The T_x of the $Ca_{32}Mg_{12}Zn_{38}Yb_{14}B_2Au_2$ sample decreases to 423 K, while the T_g has no significant change. The T_p temperature values for the $Ca_{32}Mg_{12}Zn_{38}Yb_{18-x}B_xAu_x$ (x = 1, 2) plates were 437, 466, 540 K for x = 1, and 445, 464, 537 K for x = 2, respectively.

The supercooled liquid region ($\Delta Tx = T_x - T_g$) value of the $Ca_{32}Mg_{12}Zn_{38}Yb_{14}B_2Au_2$ alloy is a little lower than that of x = 1 sample, which shows that the increasing the amount of Au does not reduce the glass-forming ability of $Ca_{32}Mg_{12}Zn_{38}Yb_{18-2x}B_xAu_x$ (x = 1, 2) alloys. When we compare the studied alloys with $Ca_{32}Mg_{12}Zn_{38}Yb_{18-x}B_x$ (x = 1, 2, 3) alloys, we can notice that the T_x temperature is in the range of 419–422 K [34].

The results of the Vickers hardness tests conducted for $Ca_{32}Mg_{12}Zn_{38}Yb_{18-2x}B_xAu_x$ (x = 1, 2) alloys are shown in Table 3. The obtained results of the hardness measurements indicate that they are higher than the hardness values reported in refs [35,36] for cortical and trabecular bone.

Table 1
ICP-AES analysis parameters and emission lines.

Operating conditions						
RF power	1.0 kW					
Plasma flow (argon)	15 L·min^{-1}					
Auxiliary flow (argon)	1.5 L·min^{-1}					
Nebulizer pressure	210 kPa					
Pump rate	15 rpm					
Wavelenght	**Au**	**B**	**Ca**	**Mg**	**Zn**	**Yb**
λ, nm	242.794	49.678	318.127	202.582	202.548	328.937
λ, nm	267.594	249.772	422.673	279.078	206.200	369.419
λ, nm				280.270	213.857	
λ, nm				383.829		

Table 2
Results of WDS analysis of $Ca_{32}Mg_{12}Zn_{38}Yb_{18-2x}B_xAu_x$ (x = 1, 2) alloy.

Sample	B [at.%] ± 0.1	Mg [at.%] ± 0.1	Ca [at.%] ± 0.2	Yb [at.%] ± 0.3	Zn [at.%] ± 0.2	Au [at.%] ± 0.1
x = 1	2.39	11.38	32.23	16.37	36.61	1.02
x = 2	2.38	11.18	32.64	14.50	37.22	2.08

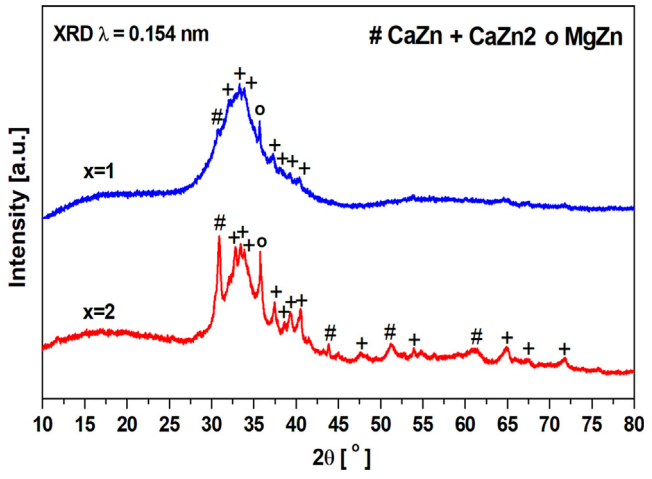

Fig. 2. XRD patterns of $Ca_{32}Mg_{12}Zn_{38}Yb_{18-2x}B_xAu_x$ (x = 1, 2) plates in as-cast state.

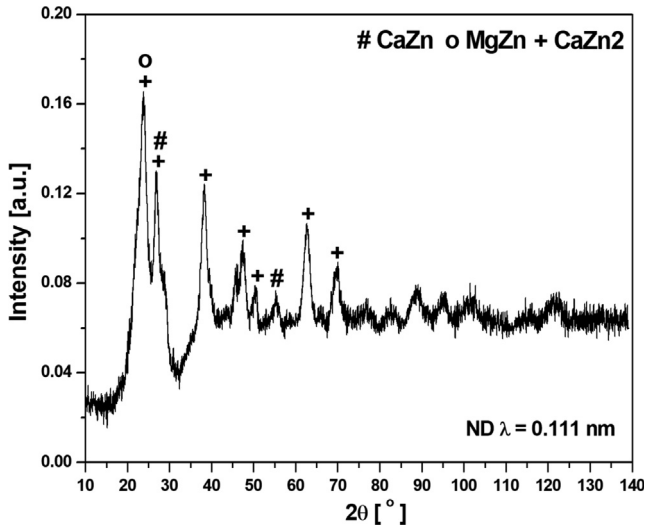

Fig. 3. ND pattern of $Ca_{32}Mg_{12}Zn_{38}Yb_{16}B_1Au_1$ plate in as-cast state.

The compressive curves of three samples for each alloy are presented in Fig. 6. The compressive strength (R_c) of $Ca_{32}Mg_{12}Zn_{38}Yb_{18-2x}B_xAu_x$ (x = 1, 2) alloys were determined as 132.5 ± 0. 5 MPa and 161 ± 4 MPa, respectively. The results are comparable with those from cortical femur bone, bovine cortical bone, and models of cortical bone for adults and children, which were shown in ref [37]. Havaldar et al. [38] reported that the compressive strength of cortical femur bone from males achieved 141.6 MP a ± 15.91 MPa. Moreover, bovine cortical bone subjected to a compressive test gave 250–400 MPa [39]. The fracture strength of $Ca_{32}Zn_{38}Mg_{12}Yb_{18}$ is 613 MPa [26]. This value is much higher than reported in ref [38]. The higher values of compressive strengths and hardness noted for $Ca_{32}Mg_{12}Zn_{38}Yb_{14}B_2Au_2$ alloy are most likely due to a higher quantity of the nanocrystalline phases in the amorphous matrix, which was noted for this sample. Metallic glassy alloys are strong and also very brittle, but the presence of nanocrystalline phases in small quantities can enhanced their mechanical properties [40]. Moreover, the addition of Au likely influences the mechanical properties.

The evolution of hydrogen (H_2) from Ringer's solution was monitored over 30 days (720 h) for both alloys (Fig. 7). The maximum amount of evolved H_2 was ~ 0.4 ml/cm^2 for the $Ca_{32}Mg_{12}Zn_{38}Yb_{16}B_1Au_1$ alloy and ~ 0.5 ml/cm^2 for the sample of $Ca_{32}Mg_{12}Zn_{38}Yb_{14}B_2Au_2$ after 720 h. The volume of H_2 after 30 days never exceeded 1 ml/cm^2. This amount is permitted for rats with a weight of 240 g. Therefore, for the proposed $Ca_{32}Mg_{12}Zn_{38}Yb_{18-x}B_xAu_x$ alloys (x = 1, 2), the decreasing trend of H_2 evolution as a function of time is noteworthy. Furthermore, human bone tissue can dissolve more hydrogen than is produced from samples [41]. Furthermore, the calculated weight loss of the corrosion rate (V_{corr}) is presented in Fig. 7b. The tendency of V_{corr} in a function of time is corresponding with values presenting H_2 evolution, however, we can observe a slight increasing behaviour. The average V_{corr} after 312 h is noted as 0.35 and 0.32 g/m^2 · h for the $Ca_{32}Mg_{12}Zn_{38}Yb_{16}B_1Au_1$ and $Ca_{32}Mg_{12}Zn_{38}Yb_{14}B_2Au_2$ alloy, adequately.

The variation in the open-circuit potential (E_{OCP}) over time of the studied alloys was monitored in Ringer's solution at 37 °C over 3600 s (Fig. 8). The E_{OCP} results for $Ca_{32}Mg_{12}Zn_{38}Yb_{18-2x}B_xAu_x$ (x = 1, 2) alloys were −1238 and −1221 mV vs. SCE, respectively. These results are higher than for Mg (−1717 mV), $Ca_{60}Mg_{15}Zn_{25}$ (−1553 mV) alloy [42], $Ca_{65}Mg_{10}Zn_{25}$ alloy (−1568 mV) [43], and also for $Ca_{32}Mg_{12}Zn_{38}Yb_{18}$ alloy (−1305 mV) [43], but are lower than for Zn (−1221 mV).

Corrosion current density (j_{corr}), corrosion potential (E_{corr}), and polarization resistance (R_p) were measured using open-circuit configurations (Fig. 9, Table 4). The E_{corr} values of the $Ca_{32}Mg_{12}Zn_{38}Yb_{18-2x}B_xAu_x$ (x = 1, 2) alloys were −1305 and −1260 mV, respectively. These were similar to the results (−1.345 V) determined for the $Ca_{32}Mg_{12}Zn_{38}Yb_{18}$ alloy [43]. The results for j_{corr} obtained for the $Ca_{32}Mg_{12}Zn_{38}Yb_{18-2x}B_xAu_x$ (x = 1, 2) alloys were 18.46 and 8.79 μA/cm^2, respectively, which is lower than for pure Mg (47.85 μA/cm^2) and Zn (33.96 μA/cm^2).

The R_p results obtained for $Ca_{32}Mg_{12}Zn_{38}Yb_{18-2x}B_xAu_x$ (x = 1,2) alloys were 0.67 and 1.82 kΩcm^2, respectively. They are higher than the results (0.32 kΩcm^2) obtained for the $Ca_{32}Mg_{12}Zn_{38}Yb_{18}$ alloy [43] and were better to those determined for $Ca_{32}Mg_{12}Zn_{38}Yb_{18-x}B_x$ (x = 1, 2, 3) alloys (R_p = 54.3, 626.7, and 497.8 Ωcm^2). The results showed that the $Ca_{32}Mg_{12}Zn_{38}Yb_{14}B_2Au_2$ alloy exhibits the most noble corrosion potential and the lowest corrosion current density. The better electrochemical parameters of these samples are probably due to the higher content of B and Au addition (2 at.%). Moreover, the thick layer of the corrosion product contained hydroxides, oxides and carbonate films forms a barrier that protects the surface and increases the resistance to corrosion. Jamesh et al. [44] stated that the Mg-Zn-Mn alloy (ZM21 Mg) shows a lower corrosion resistance than pure Mg at the initial stage in Ringer's solution. $CaCO_3$ film formation occurs on the surface of the pure Mg and ZM21 Mg alloy after immersion in Ringer's solution caused an improvement in corrosion resistance.

The EIS measurements of tested alloys and pure Mg and Z were conducted in Ringer's solution after open-circuit measurements over a time (1 h) required to stabilize the E_{OCP} potential (Fig. 10). The diameter of the semicircle of $Ca_{32}Mg_{12}Zn_{38}Yb_{14}B_2Au_2$ observed

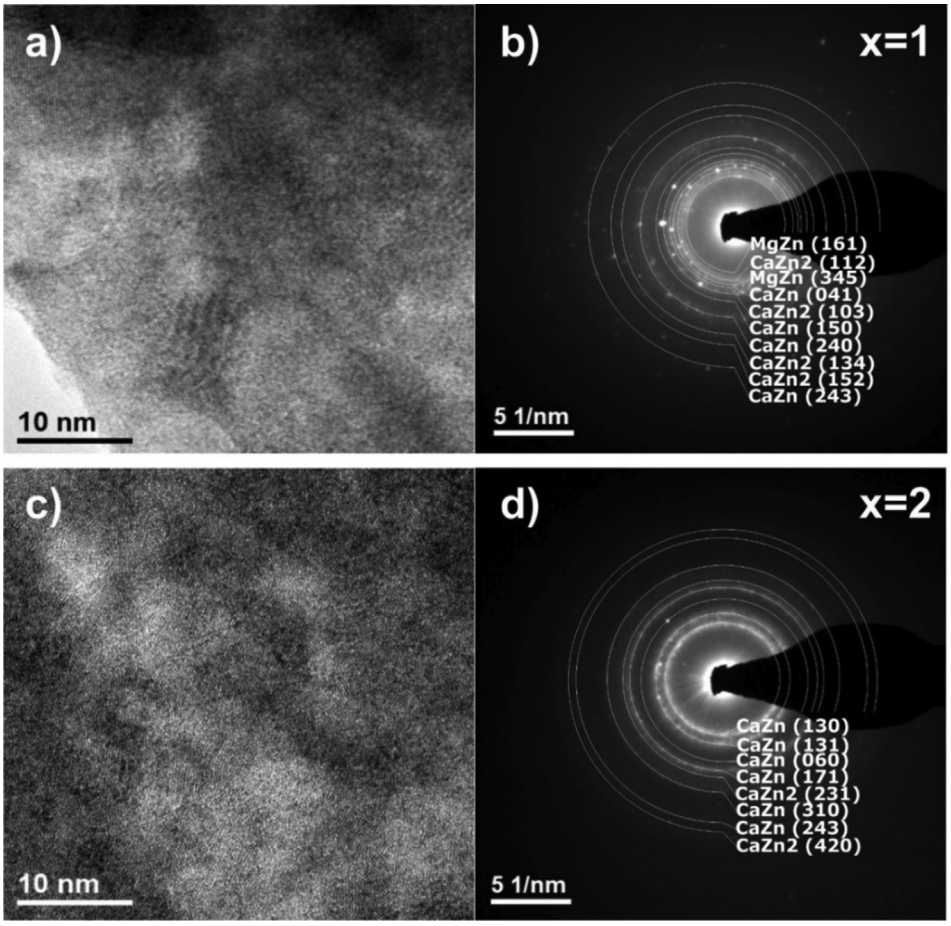

Fig. 4. HRTEM micrographs (a, c) and SAED patterns (b, d) of $Ca_{32}Mg_{12}Zn_{38}Yb_{18-2x}B_xAu_x$ (x = 1, 2) plates in as-cast state.

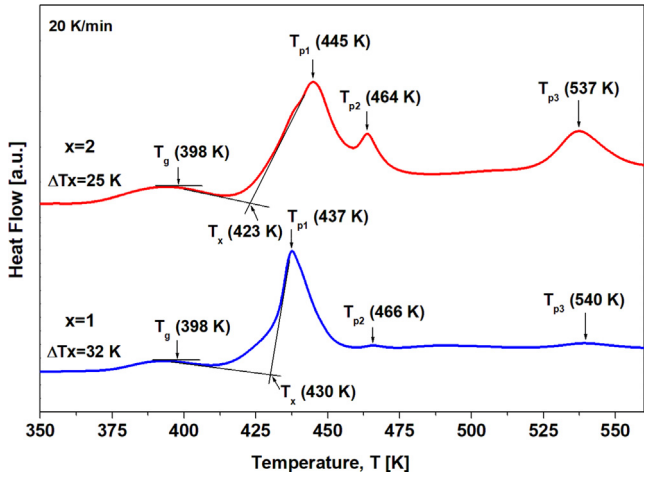

Fig. 5. DSC traces of $Ca_{32}Mg_{12}Zn_{38}Yb_{18-2x}B_xAu_x$ (x = 1,2) plates in as-cast state.

Table 3
Mechanical properties of $Ca_{32}Mg_{12}Zn_{38}Yb_{18-2x}B_xAu_x$ (x = 1, 2) plates in as-cast state (R_c – compressive strength, *HV* – Vickers hardness).

Sample	R_c [MPa]	*HV*
x = 1	132.5 ± 0.5	208 ± 2
x = 2	161 ± 4	264 ± 4

from Nyquist plots (Fig. 10a) was higher compared to that of the $Ca_{32}Mg_{12}Zn_{38}Yb_{16}B_1Au_1$ alloy, confirming the increase in the corrosion resistance of the alloy with Au addition. For comparison the Nyquist diagrams of pure Mg and Zn were added. It is clear from Nyquist plots that the diameter of the semicircle for $Ca_{32}Mg_{12}Zn_{38}Yb_{18-2x}B_xAu_x$ plates is higher comparing to pure Mg and Zn. It indicates the improvement of the corrosion resistance in Ringer's solution. The Bode-modulus plots (Fig. 10b) showed that the impedance of $Ca_{32}Mg_{12}Zn_{38}Yb_{18-x}B_xAu_x$ (x = 1,2) alloys was about 4 x 10^3 Ωcm^2 at low frequencies. In the same frequency range, the impedance of $Ca_{32}Zn_{38}Mg_{12}Yb_{18}$ alloy glasses decreased over the range of 10^3 Ωcm^2 to 10^2 Ωcm^2 for $Ca_{55}Mg_{20}Zn_{25}$ and $Ca_{65}Mg_{10}Zn_{25}$ alloys [43]. The maximum value of the Bode-phase angle (about -50°) was noted for $Ca_{32}Mg_{12}Zn_{38}Yb_{18-x}B_xAu_x$ (x = 1,2) alloys, with the response of solution resistance at a frequency of about 0.5 Hz (Fig. 10c).

Based on the attained shapes of the EIS plots, which are characterized by two time constants, an electric equivalent circuit was proposed [45,46]. The NOVA ver. 1.11.2 software was used in a simulations of impedance parameters. Experimental and simulated results using a Warburg component are shown in Fig. 11 a,b,c. The proposed equivalent circuit model is presented in Fig. 11d.

The circuit consists of solution resistance (R_s), charge transfer resistance ($R_{1,2}$), and constant phase element ($CPE_{1,2}$) and Warburg impedance (W) and tangent hyperbolic (T). The EIS parameters of $Ca_{32}Mg_{12}Zn_{38}Yb_{18-x}B_xAu_x$ (x = 1,2) were calculated after fitting the EIS spectra (Table 5). R_1 and R_2 are related to the resistances for charge transfer of the porous layer and barrier layer, adequately. CPE_1 represents the capacitance associated with porous

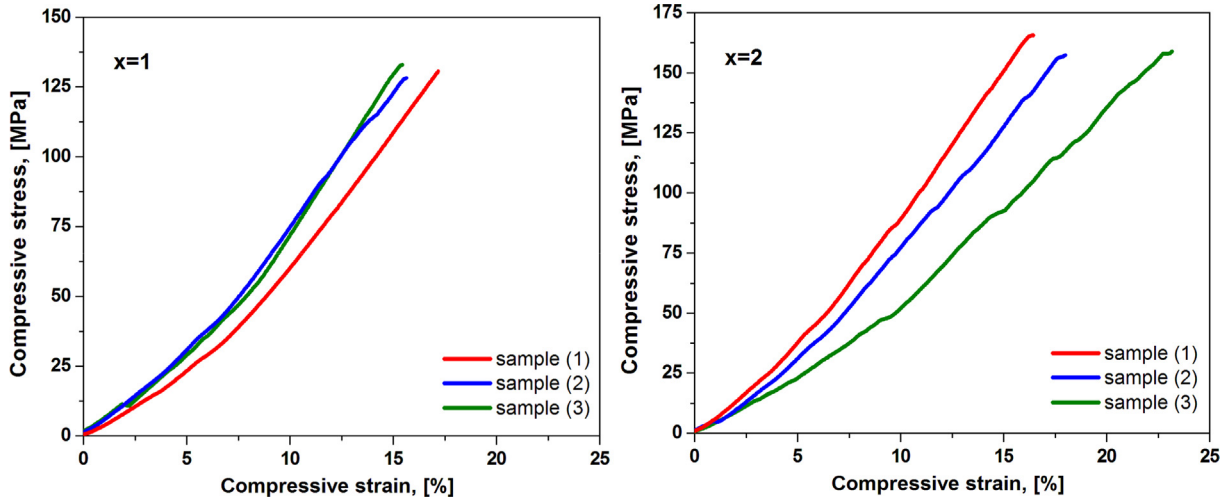

Fig. 6. Compressive curves of $Ca_{32}Mg_{12}Zn_{38}Yb_{18-2x}B_xAu_x$ (x = 1, 2) plates in as-cast state.

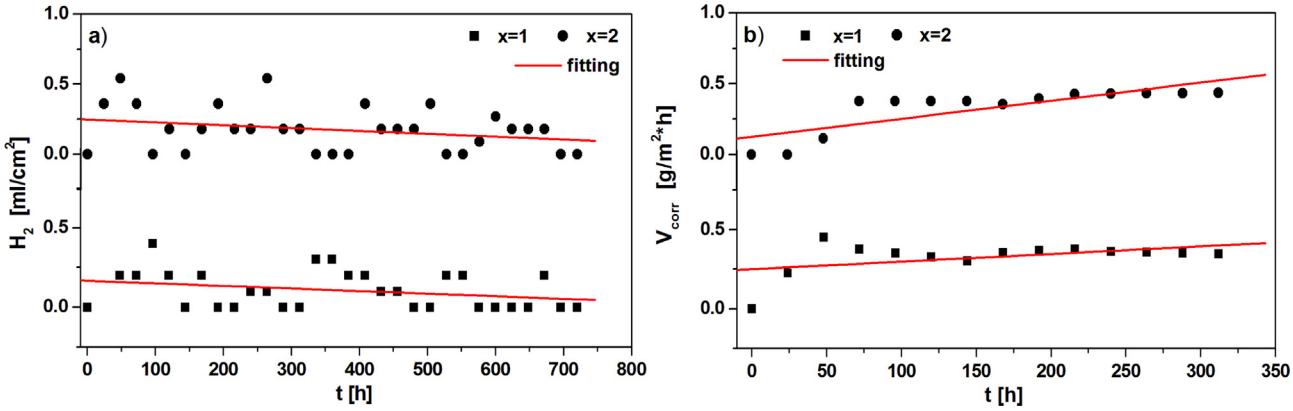

Fig. 7. Hydrogen evolution volume (a) and corrosion rate (b) over time for $Ca_{32}Mg_{12}Zn_{38}Yb_{18-2x}B_xAu_x$ (x = 1, 2) plates in Ringer's solution at 37 °C.

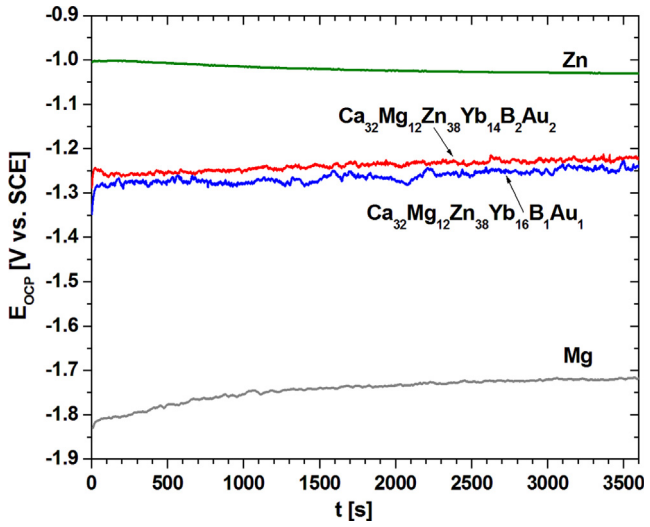

Fig. 8. E_{OCP} measurements for $Ca_{32}Mg_{12}Zn_{38}Yb_{18-2x}B_xAu_x$ (x = 1, 2) plates compared with Mg and Zn.

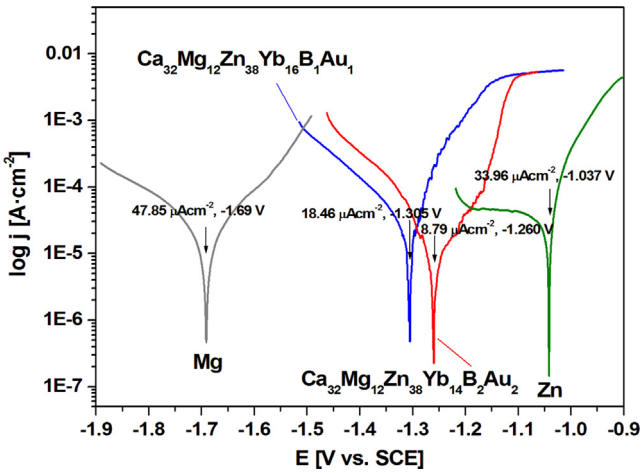

Fig. 9. Tafel plots for $Ca_{32}Mg_{12}Zn_{38}Yb_{18-2x}B_xAu_x$ (x = 1, 2) plates compared with Mg and Zn in Ringer's solution at 37 °C.

layer, CPE_2 is the double layer capacitance. W can be assumed as an impedance correlated with a diffusion process [45]. T element is also called as bounded Warburg, which is typical for porous electrodes [47].

XPS measurements that represent the surface components can be seen in Fig. 12. The characteristic photoemission and Auger peaks corresponding to individual elements are denoted. All the characteristic peaks are denoted as C1s, O1s, O2s, Mg1s, Mg2s, Ca2s, Zn3s, Ca2p, Zn2p (1/2, 3/2), and overlapped Yb4d/B1s. It

Table 4
Electrochemical properties obtained from polarization curves for $Ca_{32}Mg_{12}Zn_{38}Yb_{18-2x}B_xAu_x$ (x = 1, 2) alloys in Ringer's solution at 37 °C.

Sample	Open-circuit potential (E_{OCP}) [mV]	Corrosion potential (E_{corr}) [mV]	Corrosion current density (j_{corr}) [μA/cm^2]	Corrosion resistance (R_p) [kΩcm^2]
Pure Mg	−1717 ± 35	−1690 ± 30	47.85 ± 0.03	1.30 ± 0.03
Pure Zn	−1031 ± 20	−1037 ± 20	33.96 ± 0.3	0.37 ± 0.01
$Ca_{32}Mg_{12}Zn_{38}Yb_{16}B_1Au_1$	−1238 ± 25	−1305 ± 30	18.46 ± 0.3	0.67 ± 0.02
$Ca_{32}Mg_{12}Zn_{38}Yb_{14}B_2Au_2$	−1221 ± 25	−1260 ± 30	8.79 ± 0.2	1.82 ± 0.03

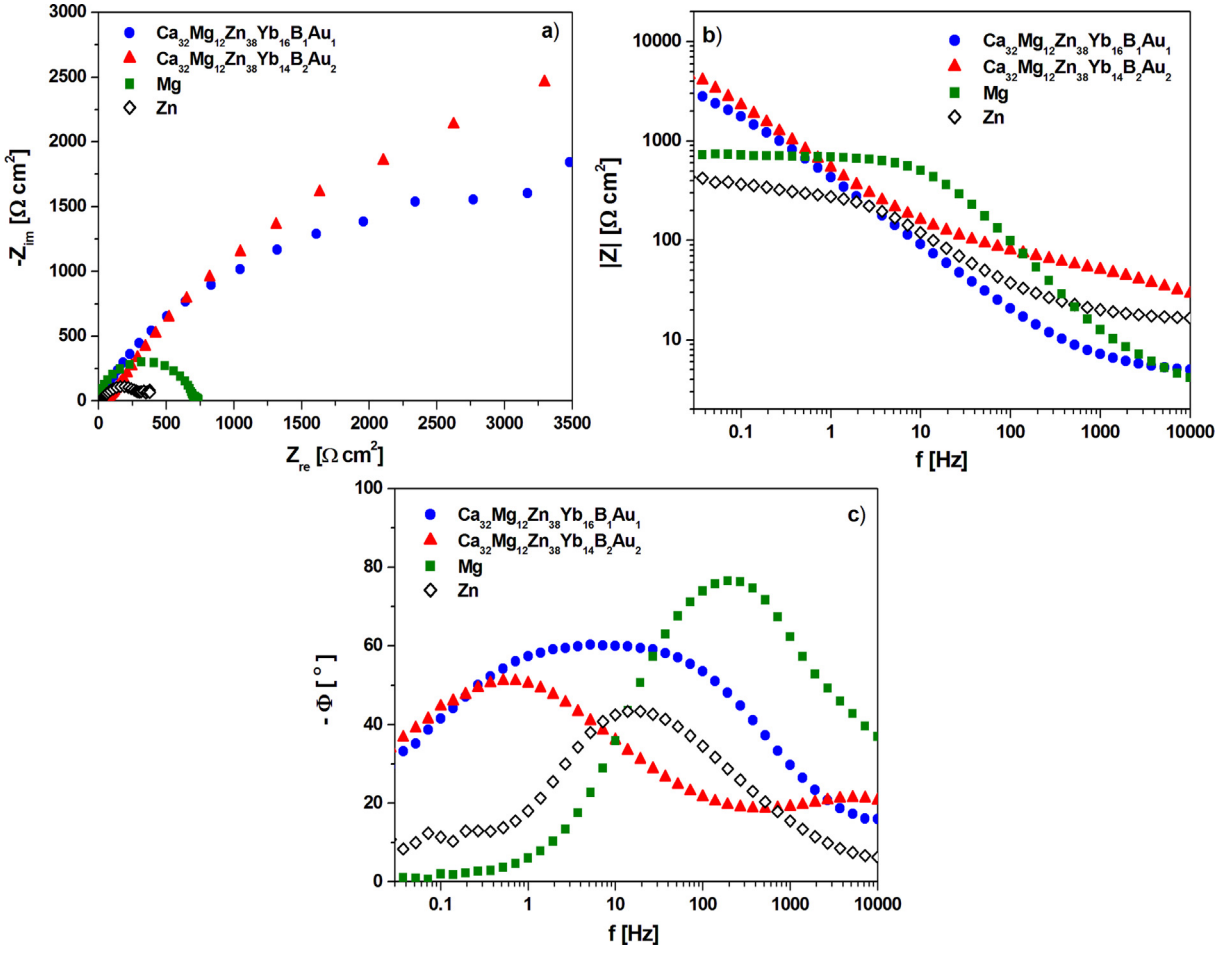

Fig. 10. Experimental EIS spectra: Nyquist plots (a), Bode modulus plots (b), Bode phase angle plots (c) for $Ca_{32}Mg_{12}Zn_{38}Yb_{18-2x}B_xAu_x$ (x = 1,2) and pure Mg, Zn plates in Ringer's solution at 37 °C.

should be noted that the dominated component on the surface is O1s, probably related to the various oxides present. The Na1s line originating from Ringer's solution could not be seen [48].

The analysis of individual core level lines seen on ion etching by an argon beam are presented in Figs. 13 and 14 for samples of $Ca_{32}Mg_{12}Zn_{38}Yb_{16}B_1Au_1$ and $Ca_{32}Mg_{12}Zn_{38}Yb_{14}B_2Au_2$ alloy, respectively, following the corrosion test in Ringer's solution at 37 °C. The first two spectra measured for each line generally having the lowest intensity (except for O1s and C1s lines) represent the surface, whereas the others enhancing the changes in chemical states represent the chemical environment of the surface underneath. The depth resolution is referred to the total sputtering time of 240 min.

During the analysis of the C1s core level line, two main peaks can be observed (Fig. 13a, 14a). The peak with the highest intensity is related to carbon accumulated on the sample surface (BE ≈ 284.8 eV), whereas the low-intensity line at the higher binding energy (BE ≈ 289.4 eV) may originate from various carbonates, probably mostly from $CaCO_3$. The carbonate peak is rather stable during the Ar etching process, whereas the main peak is drastically reduced.

The O line O1s (Fig. 13b, 14b) for both samples is quite complex. The peak located at 528.8–530.1 eV can be ascribed to lattice oxygen (O_2^{2-}), the peak situated around 531.5 eV can be assigned to the surface-adsorbed oxygen (O^{2-} or O^-), OH groups, and oxygen vacancies, and the peak at high binding energy around 534.0 eV may be associated with adsorbed water. The lattice oxygen may originate from various oxides, such as Yb_2O_3, ZnO, MgO, and CaO. The presence of oxides was clearly visible just after the first ion cleaning.

The Ca2p lines for both the studied samples differed significantly (Fig. 13c, 14c). For the $Ca_{32}Mg_{12}Zn_{38}Yb_{14}B_2Au_2$ alloy, quite broad lines around 347.4 eV and 350.9 eV with ΔE ≈ 3.9 eV, typical for $CaCO_3$, could be observed. Both lines became even broader during the sputtering procedure, and the splitting was slightly reduced, which may suggest the additional isolation of pure Ca.

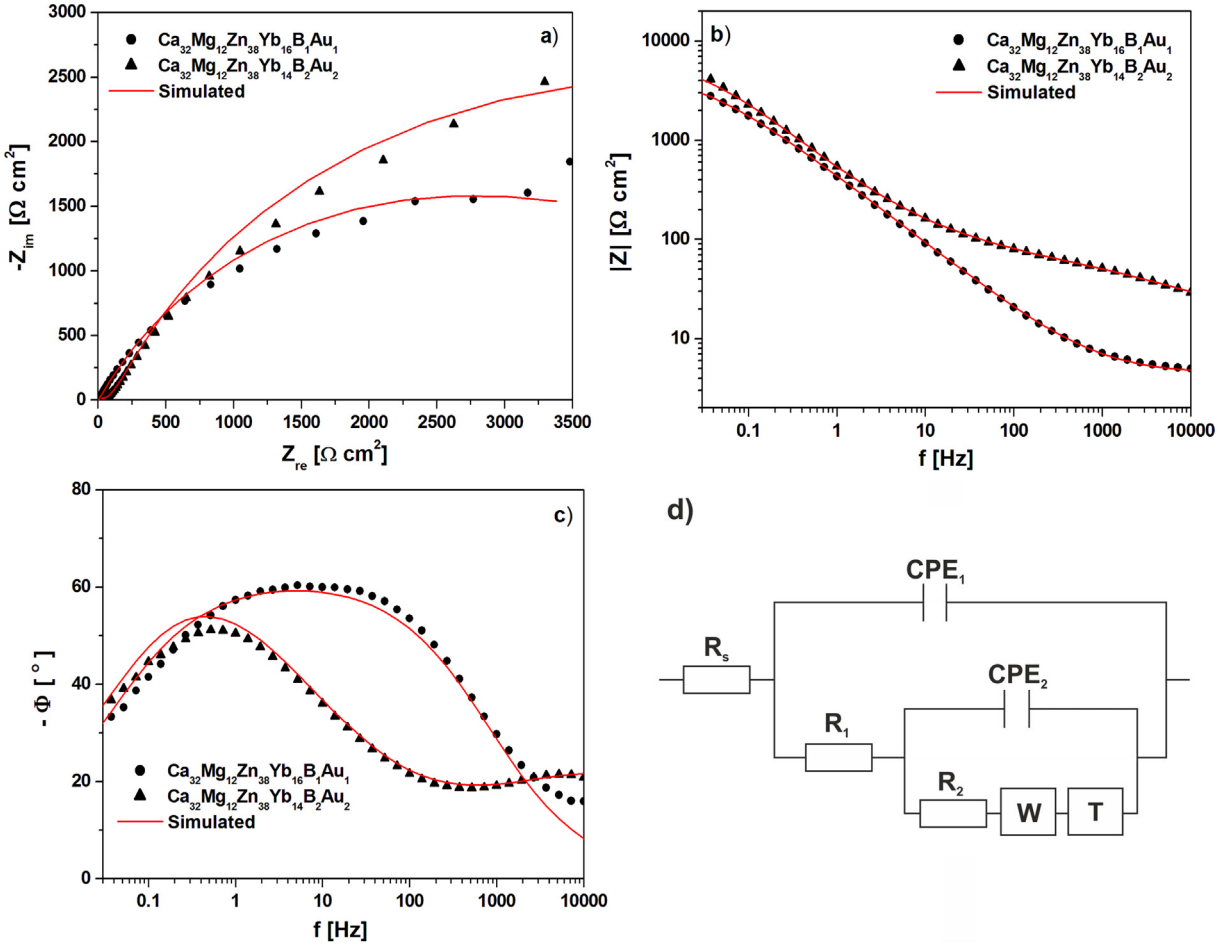

Fig. 11. Comparison of EIS spectra containing experimental and simulated results of: Nyquist plots (a), Bode modulus plots (b), Bode phase angle plots (c), proposed equivalent circuit (d) for $Ca_{32}Mg_{12}Zn_{38}Yb_{18-2x}B_xAu_x$ (x = 1,2) plates in Ringer's solution at 37 °C.

Table 5
Values of equivalent electric circuits for $Ca_{32}Mg_{12}Zn_{38}Yb_{18-x}B_xAu_x$ (x = 1,2) alloys in Ringer's solution at 37 °C (R_s – solution resistance, $R_{1,2}$ – charge transfer resistance, $CPE_{1,2}$ – constant phase element, W – Warburg impedance, T – tangent hyperbolic).

Parameter	$Ca_{32}Mg_{12}Zn_{38}Yb_{16}B_1Au_1$	$Ca_{32}Mg_{12}Zn_{38}Yb_{14}B_2Au_2$
R_s [Ω cm²]	4.64	26.6
CPE_1 [μMho cm²]	589.0	97.0
R_1 [Ωcm²]	55.8	18.6
CPE_2 [μMho cm²]	184.0	253.0
R_2 [Ω cm²]	50.4	71.7
W [mMho cm²]	1.25	0.97
T [mMho cm²]	15.9	16.7
χ^2	0.033	0.054

The analysis of the Ca2p (Fig. 13c) core level for $Ca_{32}Mg_{12}Zn_{38}Yb_{16}B_1Au_1$ alloy revealed a doublet line split via spin–orbit (L-S) splitting into Ca2p3/2 (BE ≈ 346.7 eV) and Ca2p1/2 (BE ≈ 349.8 eV) with ΔE ≈ 3.1 eV, which is typical for CaO. On the surface of Ca2p, an additional component around 348.8 eV, probably typical for $CaCl_2$, could be observed

The Zn2p lines for both samples varied greatly (Fig. 13d, 14d). In the case of the $Ca_{32}Mg_{12}Zn_{38}Yb_{14}B_2Au_2$ alloy, the Zn line from the surface with an L-S splitting of ΔE ≈ 23.1 eV is typical for ZnO. After ion etching, additional narrow lines at the low binding energies around 1019.2 eV ($Zn2p_{3/2}$) and 1042.3 eV ($Zn2p_{1/2}$), which could be assigned to Zn2p states, are observed. For the $Ca_{32}Mg_{12}Zn_{38}Yb_{16}B_1Au_1$ alloy, the Zn2p line was significantly different.

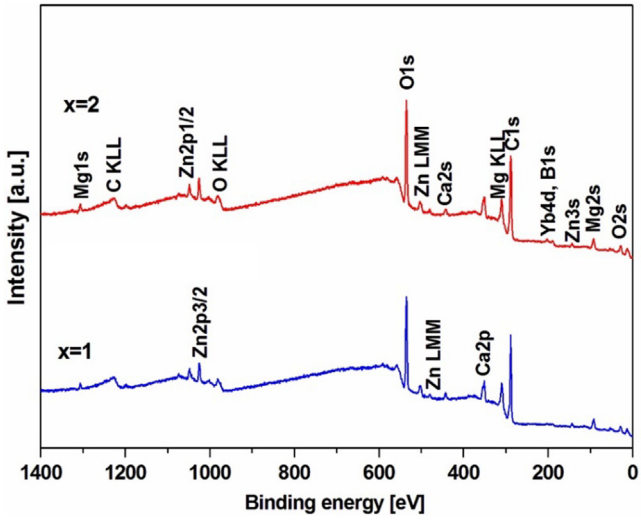

Fig. 12. XPS survey spectra for $Ca_{32}Mg_{12}Zn_{38}Yb_{18-2x}B_xAu_x$ (x = 1,2) plates after corrosion test in Ringer's solution at 37 °C.

The dominant contribution of the Zn2p states was readily noticeable.

The Yb4d doublet line (Fig. 13e, 14e) indicates L-S splitting into two main lines: $4d_{5/2}$ (BE ≈ 184.9 eV) and $4d_{3/2}$ (BE ≈ 199.1 eV), with an L-S splitting of about ΔE ≈ 14.2 eV. The main lines could

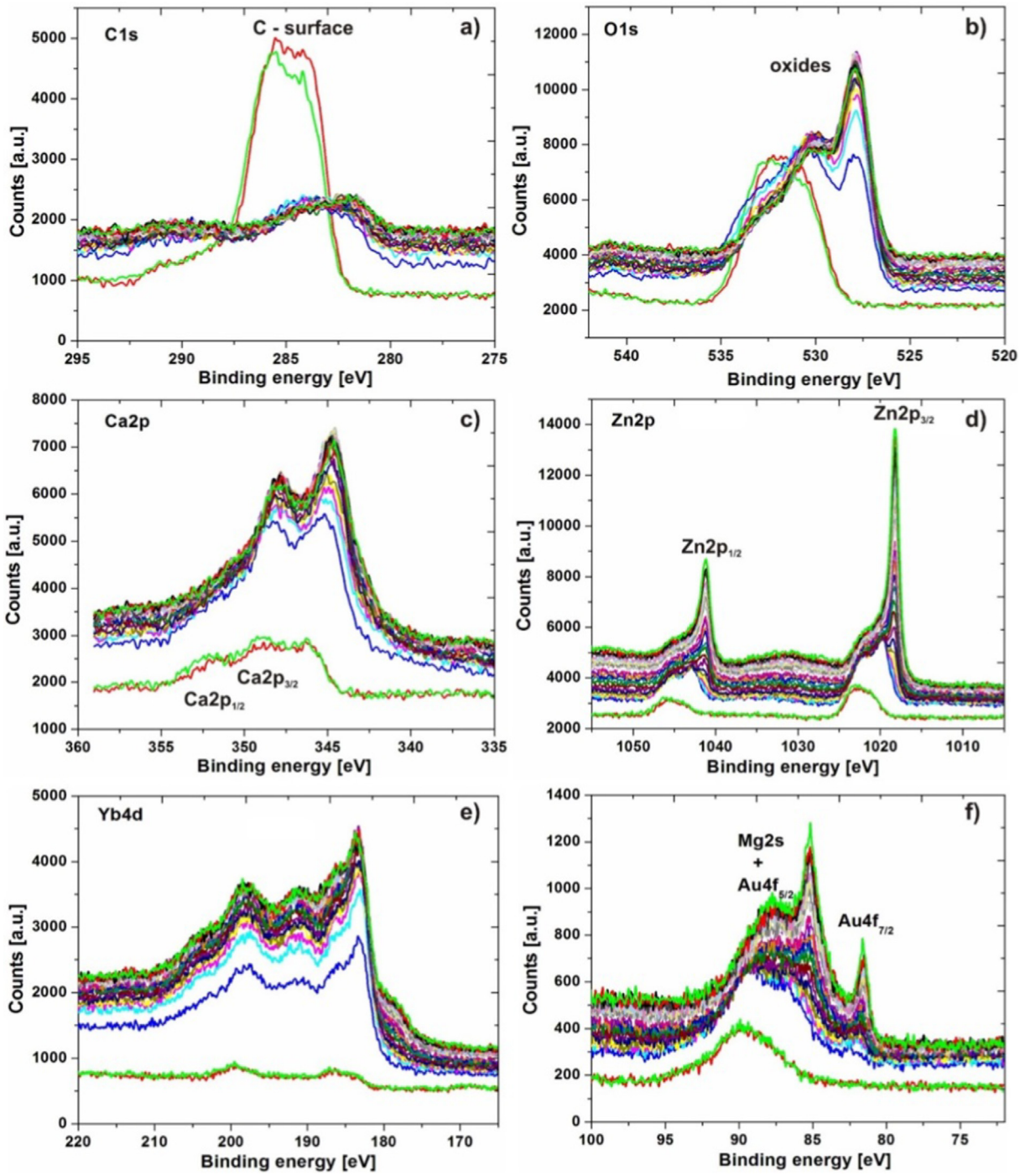

Fig. 13. Core level spectra of C1s (a), O1s (b), Ca2p (c), Zn2p (d), Yb4d (e), and Au4f (f) for $Ca_{32}Mg_{12}Zn_{38}Yb_{16}B_1Au_1$ alloy after corrosion test in Ringer's solution at 37 °C.

be assigned to Yb_2O_3. However, there is a visible additional structure at 192.3 eV and 205.1 eV. Such a complex structure with several components for the Yb4d line is typical for mixed-valence Yb3+/Yb2 + ytterbium states, suggesting a mixture of metallic and oxide states. Additionally, in the case of the B-rich sample (Fig. 13e), the presence of the B1s line (187.8 eV) as a shoulder to the Yb $4d_{5/2}$ peak is barely noticeable.

By analyzing overlapped Mg2s and Au4f lines for both samples at the surface, only the presence of the Mg2s line (BE ≈ 89 eV) can be observed. Subsequent ion etching revealed the presence of Au4f lines (Fig. 13f, 14f). The first of these, $Au4f_{7/2}$, is visible around 82.3 eV, whereas the second one, $Au4f_{5/2}$, is overlapped, not only with Mg2s but also with Zn3p, and that is why its intensity is significantly higher. It is worth noting that the gold states are typical for pure Au.

The chemical composition over sputtering time was determined based on analysis of individual core level lines having the most extensive photoemission cross-section, namely the highest intensity. Thus, the depth profiles (DP-XPS) for both measured samples were created (Fig. 15). Unfortunately, due to overlapping of Yb4d and B1s lines, it was a challenging task to determine the relative modification of the B content and which is presented jointly with Yb states. By analyzing both DP-XPS data, we may claim that the visible differences in atomic concentration modified over sputter-

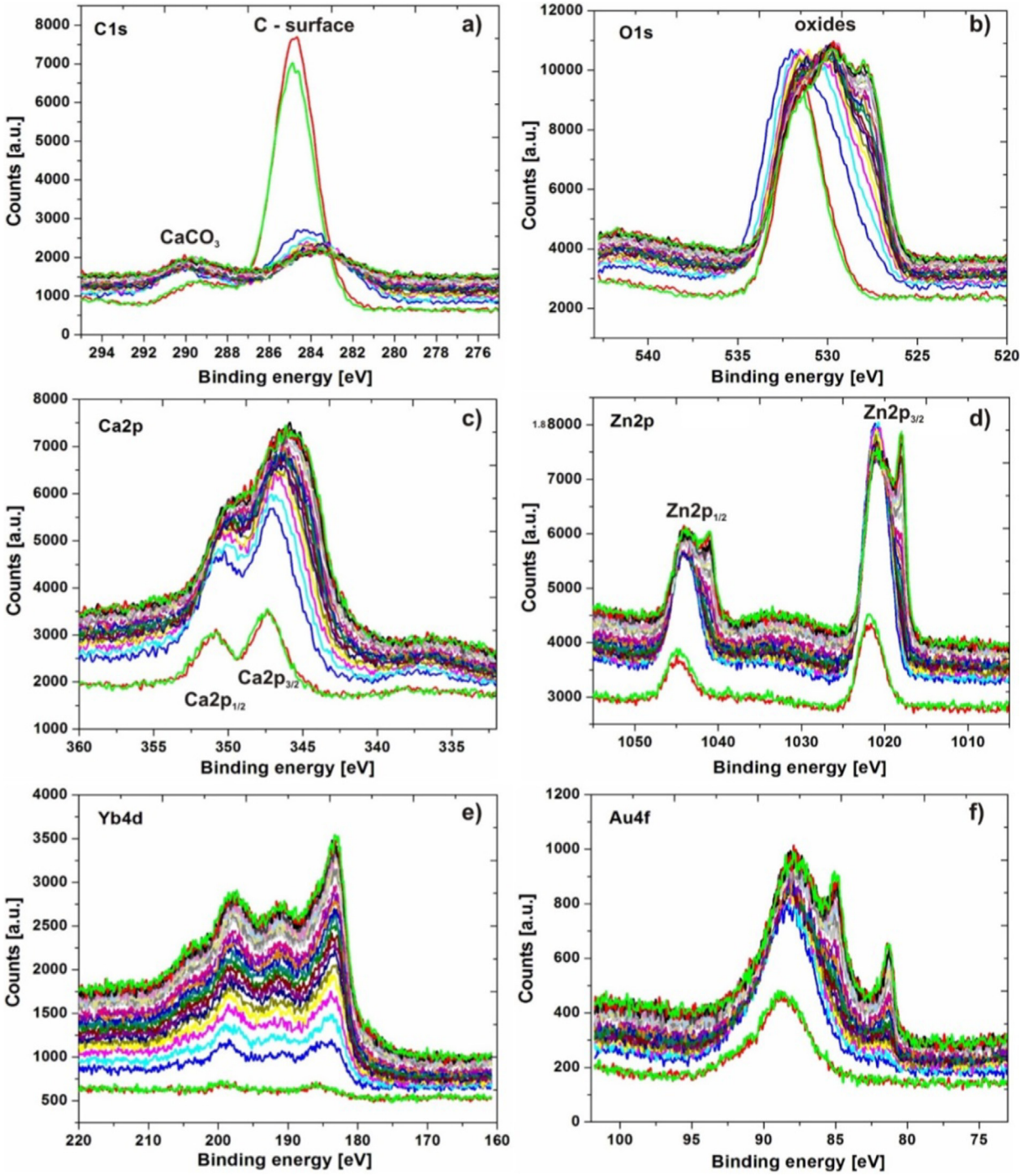

Fig. 14. Core level spectra of C1s (a), O1s (b), Ca2p (c), Zn2p (d), Yb4d (e), and Au4f (f) for $Ca_{32}Mg_{12}Zn_{38}Yb_{14}B_2Au_2$ alloy after corrosion test in Ringer's solution at 37 °C.

ing time are related to various sample formulas. For the record, the varied reaction of samples to ion etching might be due to the different local environments of atoms in both sample formulas. Thus, such phenomena cause differences in chemical shifts, e.g. well noticeable Zn2p states for both samples. Nonetheless, in both cases, dominated O1s states are associated not only to surface impurity but also to various oxides, as is evident in a detailed analysis of the core level lines. The quantity of C1s as a surface impurity is significantly reduced by the Ar beam. The noticeable difference in Yb4d + B1s amount for both samples may be associated with the various contribution in Yb2+/Yb3 + states. The lowest content was denoted for Au4f states which directly results from the formula of the tested samples.

The identities of corrosion products from the surface of plates after the 30-day corrosion tests were assigned using the XRD method (Fig. 16). The corrosion products were identified as ZnO (PDF 76–0704, P63mc), $CaCO_3$ (PDF 86–2343, R-3c), $Mg(OH)_2$ (PDF 86–0441, P-3m1), $Yb(OH)_3$ (PDF 76–1495, P63/m), $Ca(Zn(OH)_3)_2{\cdot}2H_2O$ (PDF 24–0222, P21/c) and $CaB_2O(OH)_6{\cdot}2H_2O$ (PDF 83–2027, P-1). The $CaB_2O(OH)_6{\cdot}2H_2O$ compound most likely increases the corrosion resistance of the alloys since it is slightly soluble in Ringer's solution, partially blocking further penetration

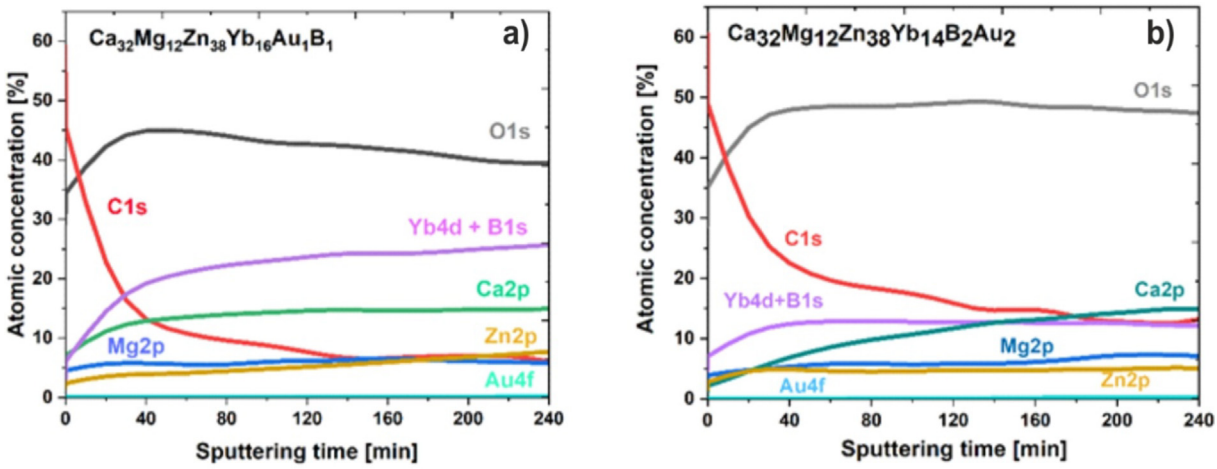

Fig. 15. Depth profiles for $Ca_{32}Mg_{12}Zn_{38}Yb_{14}B_2Au_2$ (a) and $Ca_{32}Mg_{12}Zn_{38}Yb_{14}B_2Au_2$ (b).

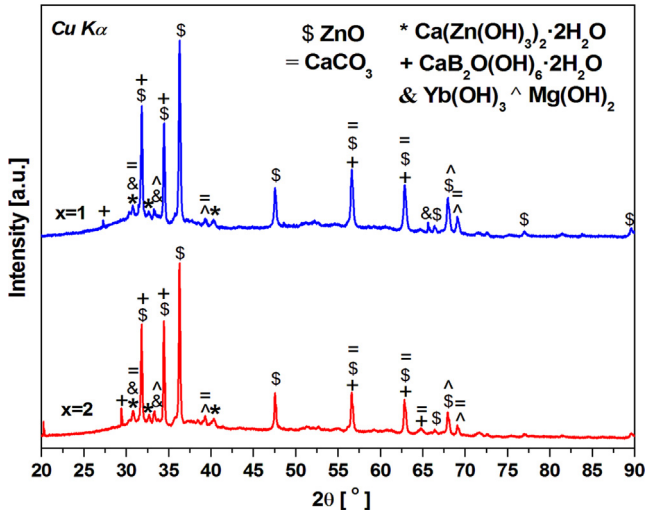

Fig. 16. XRD patterns of corrosion products of $Ca_{32}Mg_{12}Zn_{38}Yb_{18-2x}B_xAu_x$ (x = 1, 2) plates after immersion in Ringer's solution at 37 °C over 30 days.

of the solution deeper inside the alloy, and thus partially stopping corrosion.

The surface morphology of the plates after immersion in Ringer's solution at 37 °C over 7 and 30 days is presented in Figs. 17 and 18, respectively. The microscopy observations revealed the typical surface morphology with some corrosion products after aggressive corrosion attack in different chloride solutions (NaCl, KCl, and $CaCl_2 \cdot 6H_2O$). The thick corrosion product layer contained Ca and Zn hydroxide/oxide and a carbonate film. Zn oxides have a distinguishing hexagonal shape and form pillars [49,50] (Fig. 17b,d, 18b,d). The thick product layer forms a barrier film that protects the surface from further aggressive attack and increases corrosion resistance.

The concentration of the alloy's elements, such as Ca, Mg, Zn, Yb, B, and Au, in Ringer's solution before and after the immersion tests was examined using inductively coupled plasma atomic emission spectrometry (ICP-AES). The results of the ICP-AES analysis are presented in Table 6.

As suspected, the concentration of alloy's elements in Ringer's solution changed over time during immersion, along with the alloys' composition. It was observed that the Ca and Zn content in Ringer's solution increased with the immersion time. However, it was also noted that after 7 and 30 days of immersion, the Ca concentration was stable and equaled on average 97.67 mg/L. Concentration changes were observed, especially after 60 days of immersion. After this time, the Ca concentration in Ringer's solution equaled 286.51 mg/L and 276.7 mg/L for the $Ca_{32}Mg_{12}Zn_{38}Yb_{16}B_1Au_1$ and $Ca_{32}Mg_{12}Zn_{38}Yb_{14}B_2Au_2$ alloys, respectively. In comparison to Ca, the Zn concentration in Ringer's solution after the test was very small, and after 60 days immersion, did not exceed 2 mg/L. It was also found that the changes in Au, B (alloy's addition), and Mg concentrations in Ringer's solution after 7-, 30-, and 60-day immersion tests for both the investigated alloys were very similar. However, as shown in Table 6, the concentration of Mg and Yb in solution after the immersion test decreased with the increase in immersion time. The obtained results suggest that during the immersion time the dissolved Yb and Mg ions joined the corrosion reaction to form some corrosion product film. Thus it can be assumed that during examined immersion time the Mg and Yb hydroxide dissolution were not observed.

The main corrosion reactions of Mg and Yb in aqueous solution are as below [51]:

$$Mg + 2H_2O = Mg(OH)_2 + H_2 \quad (3)$$

$$2Yb + 6H_2O = 2Yb(OH)_3 + 3H_2 \quad (4)$$

The corrosion mechanism of the $Ca_{32}Mg_{12}Zn_{36}Yb_{16}B_1Au_1$ and $Ca_{32}Mg_{12}Zn_{36}Yb_{14}B_2Au_2$ alloys includes an anodic dissolution, a hydroxide precipitation, corrosion product layer formation and corrosion propagation stage (Fig. 19) [52,53]. Firstly, during the immersion in Ringer's solution (in neutral pH environment) the anodic reactions occur on the examined alloys surface. Thus, the anodic dissolution of samples were observed and the alloy's metal ions were released into the solution. Therefore the increase in concentration of alloying metal ions in solution were observed, as was confirmed in Table 6. The anodic and cathodic reactions are as below [52,53]:

$$\text{- anodic reaction: } Mg - 2e^- = Mg^{2+} \quad (5)$$

$$\text{- anodic reaction: } Ca - 2e^- = Ca^{2+} \quad (6)$$

$$\text{- cathodic reaction: } 4H_2O + 4e^- = 2H_2 + 4OH^- \quad (7)$$

In the next corrosion step, named hydroxide precipitation, the immersed samples are going to cover with a metal hydroxide. The obtained hydroxide corrosion product indicates low solubility. In Table 7 the Mg and Ca hydroxides solubilities are presented. In this step, the dissolved alloying elements joined the corrosion reac-

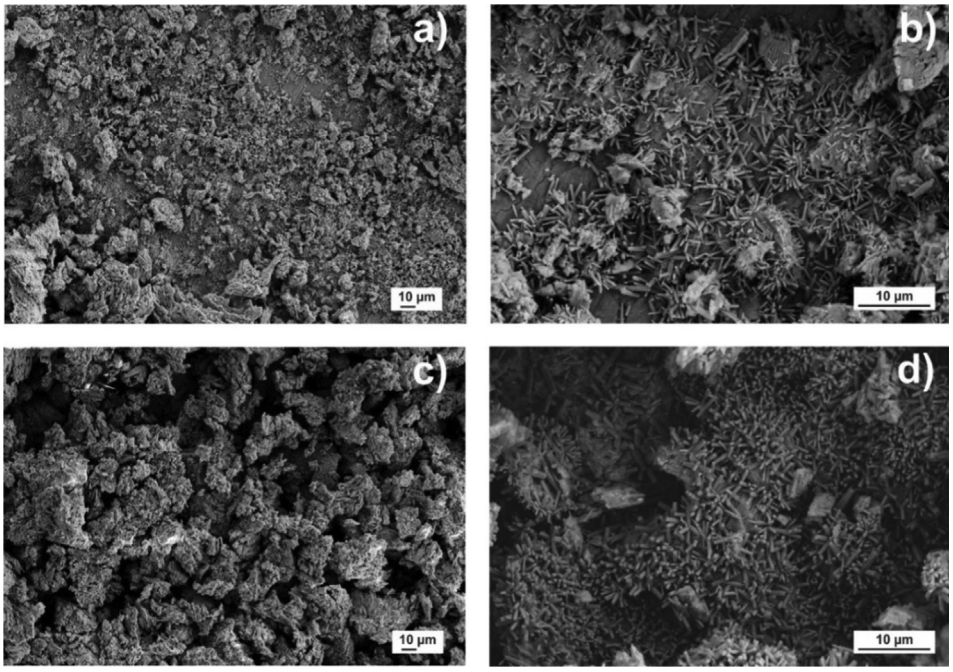

Fig. 17. Surface morphology of $Ca_{32}Mg_{12}Zn_{38}Yb_{18-2x}B_xAu_x$, x = 1 (a, b), x = 2 (c, d) plates after immersion in Ringer's solution at 37 °C over 7 days.

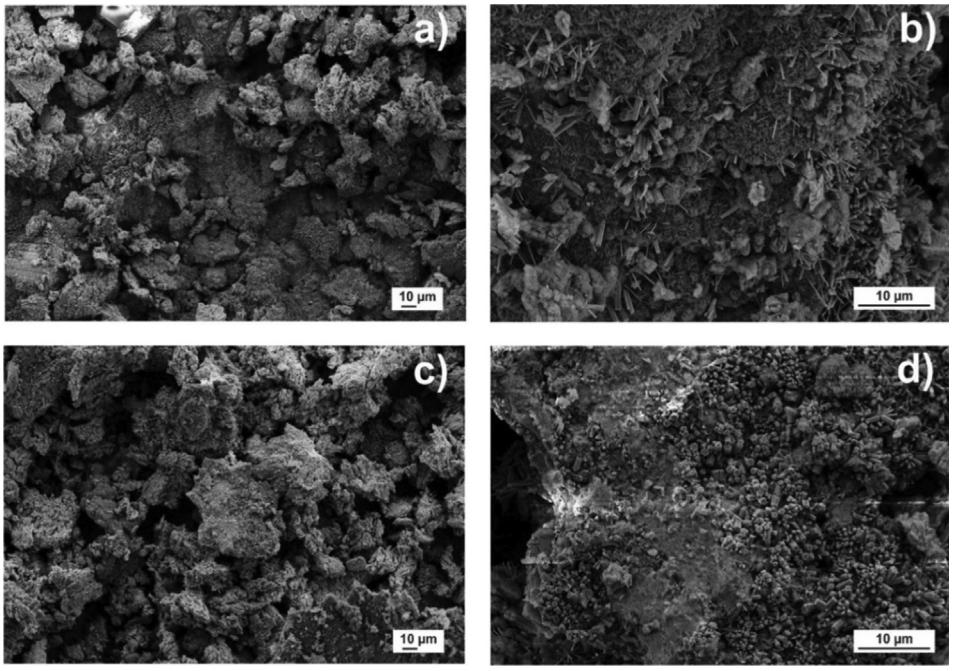

Fig. 18. Surface morphology of $Ca_{32}Mg_{12}Zn_{38}Yb_{18-2x}B_xAu_x$, x = 1 (a, b), x = 2 (c, d) plates after immersion in Ringer's solution at 37 °C over 30 days.

Table 6
The concentration of alloy elements in Ringer's solution before and after the immersion test.

Sample	Immersion time, days	Elements concentration, mg/L					
	Au	B	Ca	Mg	Yb	Zn	
Ringer's solution before immersion test	–	<0.005	<0.01	89.25	<0.01	<0.005	<0.01
$Ca_{32}Mg_{12}Zn_{35}Yb_{16}B_1Au_1$	7	0.014	<0.01	96.42	0.30	0.16	0.27
	30	0.005	<0.01	104.28	0.11	0.07	0.29
	60	0.005	0.055	286.51	0.04	0.01	1.67
$Ca_{32}Mg_{12}Zn_{35}Yb_{14}B_2Au_2$	7	0.009	0.01	97.91	0.36	0.09	0.18
	30	0.005	0.02	92.09	0.11	0.06	0.47
	60	0.005	0.05	276.7	0.04	<0.005	1.90

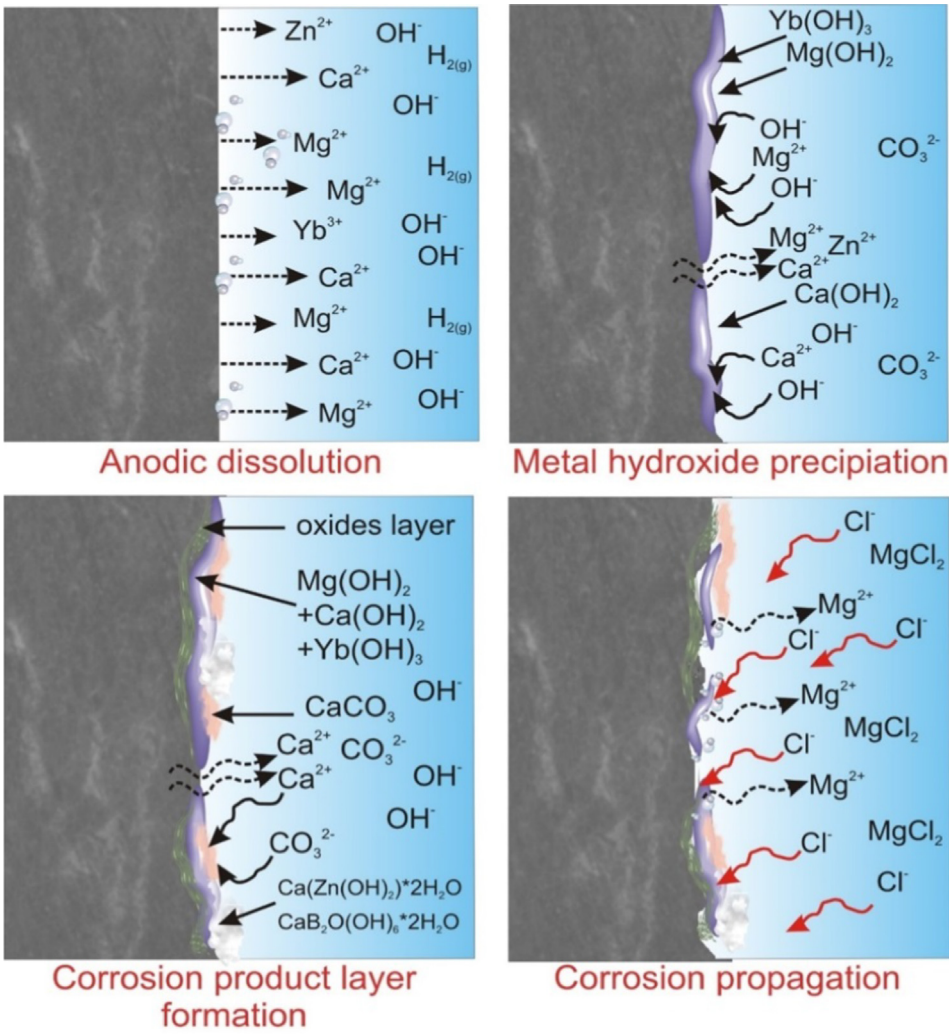

Fig. 19. Schematic presentation of a corrosion mechanism of the Ca-Mg-Zn-Yb-B-Au alloys in Ringer's solution.

tion to form hydroxides, and its concentration in solution may decrease. However the hydroxides of alloying elements are precipitated at the surface area with higher activity. What's more, it is a repeated and simultaneous process also combined with H_2 evolution. On the other hand, the Mg and Ca hydroxides form some protective layer on the alloy's surfaces. Also, the presence of carbonate ions in solution causes calcium carbonate precipitation on alloy surface. In addition, the presence of chloride ions in Ringer's solution causes their penetration and reaction with the formed hydroxide layer. This is known as the corrosion propagation stage. In this step, chloride ions react with hydroxide layer and leads to the creation of Mg and/or Ca chloride hydroxide ($Mg_x(OH)_yCl$) as follows [52]:

$$xMg^{2+} + Cl^- + yOH^- = Mg_x(OH)_yCl \quad (8)$$

The oxychlorides can occur on the alloy surface as adsorbed intermediate compounds and next they are going to dissolution as was shown below:

$$[MeCl(OH)^-] = MeClOH + e^- \quad (9)$$

$$MeClOH + H^+ = Me^{2+} + Cl^- + H_2O \quad (10)$$

The chemical composition of the Ringer's solution during immersion test depends on the corrosion mechanism of the examined alloys and particularly on the corrosion step: anodic dissolution, hydroxide precipitation and corrosion propagation. The content of alloying elements in Ringer's solution during immersion time also depends on its electrochemical activity. Mg and Ca have higher chemical activity in Ringer's solution than Zn, therefore the Zn dissolution was low.

Obtained results also indicate that, after 30 and 60 days of immersion, the H_2 evolution decreased, which is compatible with the Mg and Yb concentration changes during the immersion tests. Results of the $Ca_{32}Mg_{12}Zn_{38}Yb_{18-2x}B_xAu_x$ (x = 1, 2) alloys' degradation in Ringer's solution correspond with the XRD and XPS results obtained on the corrosion products (Fig. 16).

Ca-based alloys, due to their dissolution character, can be used as bioresorbable implants since they generate non-toxic degradation products [54]. However, the highest corrosion rate of currently known Ca-based alloys limits them in use only as orthopedic implants or vascular stents [55]. The low corrosion resistance is due to the fact that the layer of natural oxide formed on their surface is permeable, and does not form a protective barrier. One of

Table 7
Solubility of Ca and Mg hydroxides [47].

Compound	$Ca(OH)_2$	$Mg(OH)_2$
K_{sp}	5.5×10^{-6}	5.61×10^{-12}

the effective ways to improve the corrosion resistance of Ca alloys, especially Ca-Mg-Zn-(Yb,B,Au), is to achieve the homogeneous amorphous structure or modify its chemical composition by alloying additives such as noble metals (e.g. Au), rare earth elements (e.g. Yb) or metalloids (e.g. B).

Taking into account electrochemical results published in previous works [34,43], the lowest values of corrosion current density were achieved for alloys with Au addition (Table 8). The Au addition in Ca-Mg-Zn-(Yb,B,Au) alloys slows down corrosion rate and decreases H_2 evolution. The effect of B substitution for Yb on the structure and corrosion properties of $Ca_{32}Mg_{12}Zn_{38}Yb_{18-x}B_x$ (x = 0,1,2,3 at.%) alloys were reported in [34,43]. Microstructural investigations showed that $Ca_{32}Mg_{12}Zn_{38}Yb_{18}$ alloy was mainly amorphous as well as $Ca_{32}Mg_{12}Zn_{38}Yb_{16}B_2$ plates. Small reflections come from nanocrystals were detected by XRD and TEM methods for $Ca_{32}Mg_{12}Zn_{38}Yb_{17}B_1$ and $Ca_{32}Mg_{12}Zn_{38}Yb_{15}B_3$ alloys (Table 9). The Yb had a positive effect in case of an improvement of the corrosion resistance of Ca-Mg-Zn alloys in Ringer's solution. The electrochemical measurements indicated that corrosion potential decreases with the increase of B content in studied alloys. The stable tendency of evolved hydrogen as a function of immersion time was also noticed.

Based on previous research on B influence on bones, it was [14–17] decided that B should be added to Ca-based alloys. B improves bone mineralization and increases its strength by decreasing size of osteoblasts. Therefore, studied Ca-Mg-Zn-(Yb,B,Au) alloys can be proposed as implants in the form of nails and plates for use in case of fractures during the occurrence of osteopenia, i.e. early stage or advanced osteoporosis. Different types of metallic biomaterials with B addition can be also attached to other alloys, e.g. Ti-Al-V-B [12]. The increasing B content increases the repassivation potentials of Ti alloy. Higher content of osteoclast precursor cells and osteoclast activating cells were formed on surface of Ti-6Al-4 V-B alloy in comparison with base Ti-6Al-4 V alloy.

Therefore, based on the literature and experimental results, the effect of B and Au addition in $Ca_{32}Mg_{12}Zn_{38}Yb_{18-x}B_x$ (x = 0, 1, 2, 3) and $Ca_{32}Mg_{12}Zn_{38}Yb_{18-2x}B_xAu_x$ (x = 1, 2) alloys on cytotoxicity and mechanisms of cell death will be analyzed on the osteoblast-like cells (U2-OS osteosarcoma) in further work. Cells will be cultured using McCoy's 5a modified medium, supplemented with Fetal Bovine Serum (FBS), and penicillin and streptomycin. Biocompatibility experiments will be performed by indirect contact of samples.

It is worth noting that, the studies on the Ca-Mg-Zn-(Yb,B,Au) alloys, which includes the structure and properties investigations of biomaterials based on Ca, fill the gap in biomaterials engineering scientific scope. The presented research results allow for decisions to be made about the potential of the evaluated family of alloys to advance towards subsequent in vitro studies.

4. Summary

New resorbable $Ca_{32}Mg_{12}Zn_{38}Yb_{16}B_1Au_1$ and $Ca_{32}Mg_{12}Zn_{38}Yb_{14}B_2Au_2$ alloys were successfully designed and studied in order to verify their use as biomedical applications e.g. short-term implants. XPS measurements of individual core level lines revealed that the biocorrosion products formed on the surface after immersion in Ringer's solution were mostly Ca and Zn oxides, hydroxides, and carbonates. The lattice oxygen was probably related to various oxides, such as ZnO, MgO, CaO and Yb_2O_3. Ion etching revealed Yb states suggesting a mixture of metallic and oxide regions, along with the presence of B and Au.

The corrosion products identified by using the XRD method were ZnO, $CaCO_3$, $Mg(OH)_2$, $Yb(OH)_3$, $Ca(Zn(OH)_2)_3{\cdot}2H_2O$, and $CaB_2O(OH)_6{\cdot}2H_2O$. The increased corrosion resistance of Ca-Mg-Zn-Yb alloys is a result of B and Au addition. They most likely slow down the penetration of Ringer's solution by creating a barrier between Ca, B, and Cl ions. Due to the formation of Ca-B atomic pairs, an additional mechanism of increased corrosion resistance can be proposed by the growth of $CaB_2O(OH)_6{\cdot}2H_2O$ corrosion products. Moreover, during the immersion time the dissolved Yb and Mg joined the corrosion reaction to form some corrosion product film.

The H_2 evolution did not exceed 1 ml/cm^2 over 1 h. The open circuit potentials for the proposed alloys were better than for Ca-Mg-Zn alloys. The EIS parameters for the $Ca_{32}Mg_{12}Zn_{38}Yb_{18-x}B_xAu_x$ (x = 1, 2) alloys were much better than for the $Ca_{55}Mg_{20}Zn_{25}$, $Ca_{65}Mg_{10}Zn_{25}$, and $Ca_{32}Zn_{38}Mg_{12}Yb_{18}$ alloys. The controlled H_2 evolution rate was a result of the variation in the amount of B and Au in the chemical composition of studied alloys. The compressive strength and microhardness of the alloys was improved by the addition of B and Au.

Funding

The work was financed by the Rector's Grant, Silesian University of Technology, grant no.: 10/010/RGJ21/1027. The work was also supported from the statutory subsidy of the Faculty of Mechanical

Table 8
Comparison of electrochemical properties for $Ca_{32}Mg_{12}Zn_{38}Yb_{18-x}B_x$ (x = 0, 1, 2, 3) and $Ca_{32}Mg_{12}Zn_{38}Yb_{18-2x}B_xAu_x$ (x = 1,2) alloys in Ringer's solution at 37 °C.

Sample	Corrosion potential (E_{corr}) [mV]	Corrosion current density (j_{corr}) [μA/cm^2]	Corrosion resistance (R_p) [kΩcm^2]	Ref.
$Ca_{32}Mg_{12}Zn_{38}Yb_{18}$	−1345	190.0	0.32	[43]
$Ca_{32}Mg_{12}Zn_{38}Yb_{17}B_1$	−1410	356.2	0.05	[34]
$Ca_{32}Mg_{12}Zn_{38}Yb_{16}B_2$	−1313	128.9	0.63	[34]
$Ca_{32}Mg_{12}Zn_{38}Yb_{15}B_3$	−1335	174.7	0.49	[34]
$Ca_{32}Mg_{12}Zn_{38}Yb_{16}B_1Au_1$	−1305	18.46	0.67	This work
$Ca_{32}Mg_{12}Zn_{38}Yb_{14}B_2Au_2$	−1260	8.79	1.82	This work

Table 9
Comparison of structure in as-cast state and after corrosion tests in Ringer's solution at 37 °C of $Ca_{32}Mg_{12}Zn_{38}Yb_{18-x}B_x$ (x = 0,1,2,3) and $Ca_{32}Mg_{12}Zn_{38}Yb_{18-2x}B_xAu_x$ (x = 1,2) alloys.

Sample	Structure in as-cast state	Corrosion products	Method	Ref.
$Ca_{32}Mg_{12}Zn_{38}Yb_{18}$	amorphous	$Ca(OH)_2$, $Yb(OH)_3$, $CaCO_3$, $Ca[Zn(OH)_3]_2{\cdot}2H_2O$	XRD	[43]
$Ca_{32}Mg_{12}Zn_{38}Yb_{17}B_1$	amorphous with $CaZn_2$, MgZn phases	CaO, MgO, $Mg(OH)_2$, $CaCO_3$, Yb_2O_3, ZnO	XPS	[34]
$Ca_{32}Mg_{12}Zn_{38}Yb_{16}B_2$	amorphous	CaO, MgO, $Mg(OH)_2$, $CaCO_3$, Yb_2O_3, ZnO	XPS	[34]
$Ca_{32}Mg_{12}Zn_{38}Yb_{15}B_3$	amorphous with $CaZn_2$, MgZn phases	CaO, MgO, $Mg(OH)_2$, $CaCO_3$, Yb_2O_3, ZnO	XPS	[34]
$Ca_{32}Mg_{12}Zn_{38}Yb_{16}B_1Au_1$	amorphous with CaZn, $CaZn_2$, MgZn phases	ZnO, $CaCO_3$, $Mg(OH)_2$, $Yb(OH)_3$, $Ca(Zn(OH)_3)_2{\cdot}2H_2O$, $CaB_2O(OH)_6{\cdot}2H_2O$	XRD	This work
$Ca_{32}Mg_{12}Zn_{38}Yb_{14}B_2Au_2$	amorphous with CaZn, $CaZn_2$, MgZn phases	ZnO, $CaCO_3$, $Mg(OH)_2$, $Yb(OH)_3$, $Ca(Zn(OH)_3)_2{\cdot}2H_2O$, $CaB_2O(OH)_6{\cdot}2H_2O$	XRD	This work

Engineering of the Silesian University of Technology 10/010/BKM20/0384 and 10/010/BKM21/1059. Authors thank Anna Janoszka, MSc from Łukasiewicz Research Network, Institute of Non-Ferrous Metals, Gliwice, Poland for WDS analysis.

Declaration of Competing Interest

The authors declare that they have no known competing financial interests or personal relationships that could have appeared to influence the work reported in this paper.

References

[1] D. Vojtěch, J. Kubásek, J. Čapek, I. Pospíšilová, Biodegradable metallic materials for temporary medical implants, Mater. Sci. Forum 891 (2017) 395–399.
[2] I. Antoniac, R. Adam, A. Bită, M. Miculescu, O. Trante, I.M. Petrescu, M. Pogăr˘steanu, Comparative assessment of in vitro and in vivo biodegradation of Mg-1Ca magnesium alloys for orthopedic applications, Materials 14 (2021) 84.
[3] Y. Zheng, X. Gu, F. Witte, Biodegradable metals, Mater. Sci. Eng. 77 (2014) 1–34.
[4] X. Gu, Y. Zheng, Y. Cheng, S. Zhong, T. Xi, In vitro corrosion and biocompatibility of binary magnesium alloys, Biomater. 30 (2009) 484–498.
[5] J. Kubásek, D. Dvorský, J. Čapek, J. Pinc, D. Vojtěch, Zn-Mg biodegradable composite: novel material with tailored mechanical and corrosion properties, Materials 12 (2019) 3930.
[6] B. Merchant, Gold, the noble metal and the paradoxes of its toxicology, Biologicals 26 (1998) 49–59.
[7] E.T.K. Demann, P.S. Stein, J.E. Haubenreich, Gold as an implant in medicine and dentistry, J. Long Term. Eff. Med. Implants 15 (6) (2005) 687–698.
[8] A. Johnson, T. Shiraishi, Biocompatibility of precious metals for medical applications, Precious Metals Biomedical Appl. (2014) 37–55.
[9] R.W. Phillips, Skinner's science of dental materials, 9th Edition., W.B. Saunders, Philadelphia, 1991, pp. 123–133.
[10] P. Bijalwan, C. Singh, A. Kumar, K. Sarkar, N. Rani, T. Laha, A. Banerjee, K. Mondal, Corrosion behaviour of plasma sprayed Fe based metallic glass ($Fe_{73}Cr_2Si_{11}B_{11}C_3$ (at%) coatings in 3.5% NaCl solution, J. Non-Crystal. Solids 567 (2021) 120913.
[11] M.A.L. Hernandez-Rodriguez, D.A. Laverde-Cataño, D. Lozano, G. Martinez-Cazares, Y. Bedolla-Gil, Influence of boron addition on the microstructure and the corrosion resistance of CoCrMo alloy, Metals 9 (2019) 307.
[12] A. Kadhim, A. Ali, N.M. Dawood, The effect of boron addition on the microstructure and corrosion resistance of Cu-Al-Ni shape-memory alloys prepared by powder technology, IOP Conf. Ser.: Mater. Sci. Eng. 987 (2020) 012028.
[13] J. Neustadt, S. Pieczenik, Osteoporosis: beyond bone mineral density, A special report on the state of osteoporosis research, NBI Health website http://www.nbihealth.com/supporting/osteoporosisreport.pdf, 2012.
[14] F.H. Nielsen, B.J. Stoecker, Boron and fish oil have different beneficial effects on strength and trabecular microarchitecture of bone, J. Trace Elem. Med. Biol. 23 (2009) 195–203.
[15] F.H. Nielsen, S.L. Meacham, Growing evidence for human health benefits of boron, J. Evidence-Based Integr. Med. 16 (2011) 169–180.
[16] M. Eskin, Boron: An overlooked micronutrient that plays an important role in human, Vitam. & Miner. 4 (2015) 1–2.
[17] J.M. Keppel Hesselink, A.L. Russell, The role of boron salts in the treatment of symptoms in osteoartrosis: presentation of 2 cases, Juniper Online J. Case Studies 2 (2017) 001–005.
[18] E.J. Hughes, Nutritional protocol for osteoarthrosis (Degenerative Joint Disease), J. Clinical Nutrition & Dietetics 2 (2016) 1–8.
[19] S.E. Brown, 20 key nutrients for bone health - an overview, 2015. (https://www.betterbones.com/wp-content/uploads/2016/11/20keybonenutrients.pdf)
[20] M.L. Capati, A. Nakazono, K. Igawa, K. Ookubo, Y. Yamamoto, K. Yanagiguchi, S. Kubo, S. Yamada, Y. Hayashi, Biol. Trace Element Res. 174 (2016) 300–308.
[21] H. Toker, H. Ozdemir, H.B. Yuce, F. Goze, The effect of boron on alveolar bone loss in osteoporotic rats, J. Dental Sci. 11 (2016) 331–337.
[22] F.H. Nielsen, Update on human health effects of boron, J. Trace Elem. Med. Biol. 28 (2014) 383–387.
[23] L. Grausova, A. Kromka, Z. Burdikova, A. Eckhardt, B. Rezek, J. Vacik, K. Haenen, V. Lisa, L. Bacakova, Enhanced growth and osteogenic differentiation of human osteoblast-like cells on boron-doped nanocrystalline diamond thin films, PLoS ONE 6 (2011) 20943.
[24] C. Dai, S. Chen, C. Wang, L. Zhang, K. Ge, J. Zhang, Ytterbium ion promotes apoptosis of primary mouse bone marrow stromal cells?, J Rare Earths 33 (2015) 445–452.
[25] J. Wang, X. Shi, D.V. Louzguine Luzgin, H. Wu, J.H. Perepezko, Ductile biodegradable Mg-based metallic glasses with excellent biocompatibility, Adv. Functional Mater. 23 (2013) 4793–4800.
[26] W. Jiao, H.F. Li, K. Zhao, H.Y. Bai, Y.B. Wang, Y.F. Zheng, W.H. Wang, Development of CaZn based glassy alloys as potential biodegradable bone graft substitute, J. Non-Crystal. Solids 357 (2011) 3830–3840.
[27] R. Babilas, K. Cesarz-Andraczke, D. Babilas, W. Simka, Structure and corrosion resistance of $Ca_{50}Mg_{20}Cu_{30}$ bulk metallic glasses, J. Mater. Eng. Perform. 24 (1) (2015) 167–174.
[28] K. Ikarashi, T. Mizushima, A. Makino, A. Inoue, Preparation of the bulk Fe-Al-Ga-P-C-B-Si glassy alloys in a ringed form by copper mold casting, Mater. Sci. Eng. A304–306 (2001) 763–766.
[29] E. McCafferty, Validation of corrosion rates measured by the Tafel extrapolation method, Corr. Sci. 47 (2005) 3202–3215.
[30] W.R. Osório, L.C. Peixoto, D.J. Moutinho, L.G. Gomes, I.L. Ferreira, A. Garcia, Corrosion resistance of directionally solidified Al-6Cu-1Si and Al-8Cu-3Si alloys castings, Mater. Design 32 (2011) 3832–3837.
[31] X.L. Zhang, Z.H. Jiang, Z.P. Yao, Y. Song, Z.D. Wu, Effects of scan rate on the potentiodynamic polarization curve obtained to determine the Tafel slopes and corrosion current density, Corr. Sci. 52 (2009) 581–587.
[32] G. Song, A. Atrens, D. StJohn, An hydrogen evolution method for the estimation of the corrosion rate of magnesium alloys, Magn. Tech. (2001) 255–262.
[33] J. Hu, D. Huang, G. Zhang, G. Song, X. Guo, Research on the inhibitionmechanismof tetraphenylporphyrin on AZ91D magnesium alloy, Corros. Sci. 63 (2012) 367–378.
[34] D. Szyba, A. Bajorek, R. Babilas, Structural and electrochemical study of resorbable $Ca_{32}Mg_{12}Zn_{38}Yb_{18-x}B_x$ (x=1, 2, 3) metallic glasses in Ringer's solution, J. All. Comp. 815 (2020) 152313.
[35] P.B. Soares, S.A. Nunes, S.D. Franco, R.R. Pires, D. Zanetta-Barbosa, C.J. Soares, Measurement of elastic modulus and Vickers hardness of surround bone implant using dynamic microindentation - parameters definition, Braz. Dental J. 25 (2014) 385–390.
[36] X.J. Wang, X.B. Chen, P.D. Hodgson, C.E. Wen, Elastic modulus and hardness of cortical and trabecular bovine bone measured by nanoindentation, Trans. Nonfer. Metals Soc. China. 16 (2006) 744–748.
[37] G. Wang, P.K. Liaw, O.N. Senkov, D.B. Miracle, M.L. Morrison, Mechanical and Fatigue Behavior of $Ca_{65}Mg_{15}Zn_{20}$ Bulk Metallic Glass, Adv. Eng. Mater. 11 (2009) 27–34.
[38] R. Havaldar, S.C. Pilli, B.B. Putti, Insights into the effects of tensile and compressive loadings on human femur bone, Adv. Biom. Res. 3 (2014) 101.
[39] B. Yu, G.F. Zhao, J.I. Lim, Y.K. Lee, Compressive mechanical properties of bovine cortical bone under varied loading rates, J. Eng. Med. 225 (2011) 941–947.
[40] R.D. Conner, R.B. Dandliker, W.L. Johnson, Mechanical properties of tungsten and steel fiber reinforced $Zr_{41.25}Ti_{13.75}Cu_{12.5}Ni_{10}Be_{22.5}$ metallic glass matrix composites, Acta Mater. 46 (1998) 6089–6102.
[41] Y. Yan, Y. Kang, D. Li, K. Yua, T. Xiao, Y. Deng, H. Dai, Y. Dai, H. Xiong, H. Fang, Improvement of the mechanical properties and corrosion resistance of biodegradable β-$Ca_3(PO_4)_2$/Mg-Zn composites prepared by powder metallurgy: the adding β-$Ca_3(PO_4)_2$, hot extrusion and aging treatment, Mater. Sci. Eng. C 74 (2017) 582–596.
[42] R. Babilas, A. Bajorek, A. Radoń, R. Nowosielski, Corrosion study of resorbable $Ca_{60}Mg_{15}Zn_{25}$ bulk metallic glasses in physiological fluids, Prog. Natural Sci.: Mater. Inter. 27 (2017) 627–634.
[43] R. Babilas, A. Bajorek, P. Sakiewicz, A. Kania, D. Szyba, Corrosion resistance of resorbable Ca-Mg-Zn-Yb metallic glasses in Ringer's solution, J. Non-Cryst. Solids 488 (2018) 69–78.
[44] M. Jamesh, S. Kumar, T.S.N. Sankara Narayanan, Corrosion behavior of commercially pure Mg and ZM21 Mg alloy in Ringer's solution – long term evaluation by EIS, Corros. Sci. 53 (2011) 645–654.
[45] N.C. Verissimo, E.S. Freitas, N. Cheung, A. Garcia, W.R. Osório, The effects of Zn segregation and microstructure length scale on the corrosion behavior of a directionally solidified Mg-25 wt.%Zn alloy, J. All. Comp. 723 (2017) 649–660.
[46] T.A. Vida, E.S. Freitas, N. Cheung, A. Garcia, W.R. Osório, Electrochemical Corrosion Behavior of as-cast Zn-rich Zn-Mg Alloys in a 0.06M NaCl Solution, Int. J. Electrochem. Sci. 12 (2017) 5264–5283.
[47] G. Ruano, J.I. Iribarren, M.M. Pérez-Madrigal, J. Torras, C. Alemán, Electrical and capacitive response of hydrogel solid-like electrolytes for supercapacitors, Polymers 13 (2021) 1337.
[48] S.A. Abdel-Gawad, M.A. Shoeib, Corrosion studies and microstructure of Mg-Zn-Ca Alloys for biomedical applications, Surf. Interfaces 14 (2019) 108–116.
[49] A. Ananth, S. Dharaneedharan, H.J. Seo, M.S. Heo, J.H. Boo, Soft jet plasma-assisted synthesis of zinc oxide nanomaterials: Morphology controls and antibacterial activity of ZnO, Chem. Eng. J. 322 (2017) 742–751.
[50] N.H. Harun, R.B.S.M.N. Mydin, S. Sreekantan, K.A. Saharudin, K.Y. Ling, N. Basiron, F. Radhi, A. Seeni, Shape-dependent antibacterial activity against staphylococcus aureus of zinc oxide nanoparticles, Mal. J. Med. Health Sci. 14 (2018) 141–146.
[51] M. Ali, M.A. Hussein, N. Al-Aqeeli, Magnesium-based composites and alloys for medical applications: A review of mechanical and corrosion properties, J. Alloys Compd. 792 (2019) 1162–1190.
[52] E.V. Parfenova, O.B. Kulyasova, V.R. Mukaeva, B. Mingo, R.G. Farrakhov, Y.V. Cherneikina, A. Yerokhin, Y.F. Zheng, R.Z. Valiev, Influence of ultra-fine grain structure on corrosion behaviour of biodegradable Mg-1Ca alloy, Corros. Sci. 163 (2020) 108303.
[53] K. Yang, C. Zhou, H. Fan, Y. Fan, Q. Jiang, P. Song, H. Fan, Y. Chen, X. Zhang, Bio-Functional Design, Application and Trends in Metallic Biomaterials, Int. J. Mol. Sci. 19 (2018) 1–21.
[54] J.D. Cao, N.T. Kirkland, K.J. Laws, N. Birbilis, M. Ferry, Ca-Mg-Zn bulk metallic glasses as bioresorbable metals, Acta Biomater. 8 (2012) 2375–2383.
[55] M. Moravej, D. Mantovani, Biodegradable metals for cardiovascular stent application: Interests and New Opportunities, Inter. J. Mol. Sci. 12 (7) (2011) 4250–4270.